



**HAL**  
open science

## **Fault imprint in clay units: Magnetic fabric, p-wave velocity, structural and mineralogical signatures**

Eva Moreno, Catherine Homberg, Johann Schnyder, Alain Person, Christian David, Arthur Du Peloux, Emeline Moubeche, Audrey Bonnelye, Pierre Dick

### ► **To cite this version:**

Eva Moreno, Catherine Homberg, Johann Schnyder, Alain Person, Christian David, et al.. Fault imprint in clay units: Magnetic fabric, p-wave velocity, structural and mineralogical signatures. *Tectonophysics*, 2018, 745, pp.264-277. 10.1016/j.tecto.2018.07.017 . hal-02006500

**HAL Id: hal-02006500**

**<https://hal.sorbonne-universite.fr/hal-02006500v1>**

Submitted on 4 Feb 2019

**HAL** is a multi-disciplinary open access archive for the deposit and dissemination of scientific research documents, whether they are published or not. The documents may come from teaching and research institutions in France or abroad, or from public or private research centers.

L'archive ouverte pluridisciplinaire **HAL**, est destinée au dépôt et à la diffusion de documents scientifiques de niveau recherche, publiés ou non, émanant des établissements d'enseignement et de recherche français ou étrangers, des laboratoires publics ou privés.

# 1 Fault imprint in clay units: magnetic fabric, p-wave velocity, 2 structural and mineralogical signatures

3  
4 Moreno Eva<sup>1</sup>, Catherine Homberg <sup>2</sup>, Johann Schnyder<sup>2</sup>, Alain Person<sup>2</sup>, Christian David<sup>3</sup>  
5 Arthur du Peloux<sup>2,4</sup>, Emeline Moubeche<sup>2</sup>, Audrey Bonnelye<sup>3</sup>and Pierre Dick<sup>4</sup>

6 1- Sorbonne Université, Faculté des Sciences, MNHN, CNRS, IRD, IPSL, LOCEAN, F-  
7 75252 7 Paris, France.[eva.moreno@mnhn.fr](mailto:eva.moreno@mnhn.fr) (corresponding author)

8 2- Sorbonne Université, Faculté des Sciences, CNRS, IStEP, F-75252 Paris, France.

9 3-Université de Cergy-Pontoise, Laboratoire Géosciences &Environnement Cergy (GEC), F-  
10 10 95000 Neuville sur Oise, France.

11 4- Institut de radioprotection et de sûreté nucléaire IRSN/PRP-DGE/SRTG, Laboratoire d'  
12 Etude et de recherche sur les Transferts et les Interactions dans les Sols, BP 17, F-92262  
13 Fontenay13 aux-Roses Cedex, France.

## 14 **1. Introduction**

15 Because of their low permeability properties coupled to a large thickness (several hundreds of  
16 meters) and a high sorption capacity, argillaceous formations have been considered as  
17 potential host rocks for nuclear waste long-term storage in several countries (Cabrera, 2002;  
18 Matray et al. 2007; Sellin and Leupin, 2013). However, faults and fractures in these materials  
19 are likely to impair their natural containment capabilities. For this reason, understanding the  
20 hydro-mechanical properties and the behaviour of faults in clay-rich sedimentary rocks is a  
21 topical subject for better appreciating fluid migration in deep sedimentary basins and the  
22 potential loss of integrity as geological barriers (De Barros et al. 2016; Lefevre et al. 2017).

23 Anisotropy is an important characteristic that influences the clays behaviour. The properties  
24 of the argillites normally depend on the process of rock formation (deposition, compaction  
25 and diagenesis) but bedding, schistosity, and cleavage also affect the anisotropic character of

26 the clays. Anisotropy properties of argillaceous formations can be evaluated by conducting  
27 the magnetic susceptibility p-wave velocity measurements. In clay-rich sedimentary rocks  
28 formations, the anisotropy of magnetic susceptibility (AMS) technique can be used to detect  
29 very subtle to strong tectonic deformation, even when they look undeformed at outcrop scale  
30 (Parès, 2015). On the other hand, the anisotropy of p-wave velocity (APV) is mainly  
31 controlled by the bulk elastic parameters, including the effect of pores, cracks and  
32 mineralogical content (Louis et al.2008) and is strongly influenced by deformed structures  
33 such as scaly clays, shear bands and microfolds because they are small-scale discontinuities  
34 (Jaeggi et al. 2017). Therefore, the AMS and APV are two complementary approaches for  
35 understanding the effect of failures, fractures and ductile deformation in the organization of  
36 clays. Despite the interest that these two properties have in the integral understanding of the  
37 behaviour of the rock in fracturing, there are not many studies in which these two techniques  
38 are combined. Louis et al. (2008) characterized the AMS and APV in siltstones and  
39 sandstones samples in the Chelungpu fault system (Taiwan). These two techniques were also  
40 used to investigate the anisotropic behaviour of the Callovo-Oxfordian argillites (David et al.  
41 2007) but far from a fault core zone.

42 In addition, the presence of faults and fractures can play an important role in controlling the  
43 migration of crustal fluids and therefore mineralogical changes are extremely sensitive to fault  
44 architecture. The intensification of the fracture network in the damage zone leads to an  
45 increased permeability with respect to the undamaged zone conducting to an authigenic  
46 growth of clays and other minerals. Conversely, the fault gouges tend to indicate a general  
47 low bulk hydraulic conductivity behaviour (Faulkner et al. 2010; Dick et al. 2016; Lefevre et  
48 al. 2016).

49 Thus, it seems that a close-knit coupling exists between structure, mechanics and fluid flow  
50 properties in fault zones (Faulkner et al. 2010). The mechanical properties of the protolith will  
51 influence the architecture of the fault zone, which will control the fluid circulation that will  
52 itself affect the mechanical properties of the fault zone.

53 To better understand the interrelationship between fault architecture, petrophysical properties  
54 and fluid flow circulation within a fault zone in argillaceous formation, a multidisciplinary  
55 study was made in two cores horizontally cores drilled in the Tournemire underground  
56 research laboratory (URL) in southern Aveyron (France). We used an integrated approach  
57 involving: structural analysis of plane and faults, petrophysical properties (APV and AMS)  
58 and mineralogical content.

59 To our knowledge this is one of the first studies to combine petrophysical and mineralogical  
60 properties of samples retrieved across a fault core zone and thus this work provides a unique  
61 opportunity to better understand the evolution of structure, petrophysical and fluid flow  
62 properties across a fault zone within clay formations. Several important questions will be  
63 addressed: Do AMS and APV properties change in phase or is their evolution different with  
64 respect to the fault? To what extent are the AMS and APV properties related to tectonic  
65 deformation? How much are these properties sensitive to localized deformation? Is it possible  
66 to observe a mineralogical change involving the presence of fluid circulation? Is there a  
67 relationship between the mineralogical changes and the petrophysical properties of the  
68 sediment?

## 69 **2. Geological and tectonic features**

70 The Tournemire Underground Research Laboratory (URL) is located in the South of France  
71 (Aveyron) in the western part of the so-called “Causse du Larzac” (Figure 1). The URL is

72 operated by the French Institute for Radiological Protection and Nuclear Safety (IRSN), to  
73 study the confining properties of an argillaceous formation (Cabrera et al., 1999).

74 The sedimentary series in this site are composed of a 250 m thick layer of clays and marls  
75 (Toarcian and Domerian) bordered by two limestone and dolomite formations (Aalenian/  
76 Bajocian in the upper part, and Carixian/ Sinemurian in the lower part) where two aquifers  
77 are present (Cabrera et al., 1999).

78 Fracturing evolution, associated with the regional tectonic history in the Tournemire area,  
79 was described and discussed in detail by Constantin et al. (2002, 2004). To summarize, the  
80 tectonic faults and fractures observed in the region are the results of two main tectonic  
81 phases: a first extensional tectonic phase, which comprises three episodes during the  
82 Mesozoic and a second major tectonic phase occurred during the Eocene associated to the  
83 Pyrenean compression.

84 The argillaceous formation of Tournemire is affected (Figure 1) by the Cernon fault (80 km  
85 long) which present a vertical and horizontal offset of several hundreds of meters and the  
86 Tournemire fault (11 km long), a local fault associated with compression tectonics (Cabrera,  
87 2002).

88 In addition, the URL is crossed by two main parallel fault zones (F1 and F2) separated by  
89 relatively undeformed rock (Bretaudeau et al., 2014) (Figure 2A). These faults of several  
90 hundred-meter length present a small vertical but a larger horizontal displacement (strike-slip  
91 faults). The main underground tunnel and several galleries intercept these faults and several  
92 boreholes have been drilled by the IRSN. Therefore, the Tournemire URL presents a unique  
93 opportunity to study in situ the evolution of the properties of clays with respect to this type of  
94 faults.

95 Previous studies indicate that the F1 and F2 faults show mainly a reverse left-lateral strike slip  
96 movement (Peyaud et al. 2006). The fault's strike between N170° to N010° and 60°W to  
97 80°W (Lefèvre et al., 2016).

98 The sedimentary series have a sub-horizontal bedding which dips gently by 5-10° towards  
99 north but it can reach higher bedding dip values at the fault core (Dick et al., 2016). A  
100 dolomitic horizon marker crossed by several boreholes on either side of the fault indicated a  
101 perpendicular slip perpendicular of around 4–6 m while slip along strike is estimated to be  
102 between 15 and 30 m (Dick et al. 2016).

### 103 **3. Materials and strategy of sampling**

104 We studied two boreholes (called cores in this paper): core TF1 (dip 1°, azimuth 80°N) and  
105 core ASM1 (dip 0°, azimuth 70°N). They were respectively drilled in the main tunnel in 1998  
106 and in the “east gallery\_03” in 2012 (Figure 1). ASM1 measures 101 mm in diameter and  
107 690 cm in length and was entirely studied. TF1 measures 96 mm in diameter and 2000 cm in  
108 length but only the interval between 480 and 1432 cm and between 1578 and 1600 cm was  
109 studied. Most of the measurements were done on 2014 and 2015 and until that time, the  
110 section cores were kept vacuum sealed in foil to prevent sample alterations.

111 The architecture of the fault zone F2 has been already characterized in previous papers (Dick  
112 et al. 2016, Lefevre et al. 2016). It is characterized by a central fault core and a fractured  
113 damage zone. The fault core consists in thin dark bands of centimetre thick gouge, cataclastic  
114 and brecciated rocks, as well as sub-vertical schistosity planes, folds and also lenses of less  
115 deformed rocks (Dick et al., 2016). The surrounding fractured damage zone is characterized  
116 by a dense network of small faults, fractures, and calcite veins. Figure 2B shows an example

117 of the type of structures that were observed at the damage zone and the fault core zone of the  
118 TF1 fault.

119 The length of each zone in cores TF1 and ASM1 was determined on the basis of the  
120 description and the log carried out during the drilling operation (IRSN internal reports)  
121 (Figure 3). In both cores, the number of fractures was significantly higher in western side  
122 than in the eastern side. In addition, while the boundary between the damage and the fault  
123 core zone is sharp, the boundary between the damage and the undamaged zones was vague.  
124 In core TF1, the western and the eastern sides of the core measure respectively 3 m and 1 m  
125 and the fault core measures 0.8m. In core ASM1, both sides have a very similar extent of  
126 around 2.5m and the fault core measures 1m (Figure 3).

127 After the macro fracture pattern analysis, the core sections were cut in  $2 \times 2 \times 2 \text{cm}^3$  oriented  
128 cubes for the measurement of anisotropy of magnetic susceptibility (AMS, 250 samples) and  
129 the anisotropy of P-wave velocity (132 samples). Unfortunately, the section 1380-1406 was  
130 too fractured and the preparation of cubes failed.

131 Samples intended for bulk mineralogical content, clay mineral content and magnetic mineral  
132 analysis were obtained differently in the undamaged and the damaged zone. In the  
133 undamaged zone, a whole piece of the bulk sediment was cut and crushed in a mortar. In the  
134 damage zone and at the fault core fault, the samples were taken along the fracture planes.  
135 About 1 mm thick layer, was scratched and crushed in a mortar into fine (bulk mineralogy,  
136 magnetic minerals) or coarse (clay minerals content) powders.

137 **4. Results**

138 4.1 Structural analysis

139 TF1 core is cut by numerous thin fracture planes, most of them showing a well preserved  
140 striae (Figure 4A). Most of the brittle deformation within the F2 fault zone thus corresponds  
141 to fault planes. Faulting is more intense in the damage zone (67 fractures measured in the  
142 western damage zone) than in the fault core (14 fractures measured). Due the absence of  
143 weathering, the fault surfaces are exceptionally well preserved enabling to determine the  
144 sense of slip. Seventy-six fault slip data, including fault plane and slip vector (striae), were  
145 thus collected in TF1 core, as well as five fractures with no or poorly preserved striae as  
146 shown in the rose diagram, 85% of the measured fault planes trend between N150°E and  
147 N020°E, thereby confirming the N-S orientation of the F2 fault zone and further indicating a  
148 moderate variability of the brittle fracture strike within the fault zone.

149 The fault population collected in TF1 core does not fit with a unique sense of shear, revealing  
150 a complex history of F2 fault. Dextral and sinistral movements, as well as normal and reverse  
151 movements exist (Figure 4A). The two last types represent 15% and 9% of the fault planes.  
152 Strike-slip faults thus represented the majority of the measured planes (76%). Among them,  
153 dextral and sinistral faults where found in a similar proportion. The distribution direction has  
154 prominent peaks trending at N000°E -N010°E for the sinistral faults, N010°E -N020°E for the  
155 dextral and reverse faults, and N020°E -N030°E for the normal faults. This similarity in  
156 direction suggest that some faults corresponded to the reactivation of others which is further  
157 confirmed by the observation of superposed horizontal and highly dipping striae on several  
158 fault planes. The superposition seems non-systematic and a relative age-relation by striae  
159 overprinting could not be determined. Despite the age uncertainty, these data indicate that F2  
160 fault zone suffered several periods of activity under different driving stresses. Two strike-slip



161 regimes, with approximate NE-SW and NW-SE compression, and a normal regime with a  
162 WNW-ESE direction of extension are inferred from the orientation of the fault-slips.

163 The brittle fractures observed in ASM1 core are different than in TF1 core. 64% of the 36  
164 measured fracture planes in ASM1 trend between N100°E and N140°E (Figure 4B). Among  
165 the 22 fractures showing a well preserved striae, all but three correspond to reverse faults with  
166 a more or less important strike-slip component. The remaining fractures are E-W sinistral  
167 faults with or without a normal component (3 data) and WNW-ESE joints (14 data).

168 Observations carried on the gallery walls indicate that an E-W reverse fault exists close to the  
169 ASM1 drilling. We therefore suggest that most fractures measured in ASM1 core are related  
170 to this second fault. Rare NS planes exist, probably in relation with F2 fault, but this  
171 overprinting makes difficult to capture how the architecture of F2 fault evolves from ASM1 to  
172 TF1 drilling.

173 As far as the fault dips are concerned, most of the N-S fault planes collected in TF1 core,  
174 whatever their movement, show value between 5° to 45° (Figure 4A). This moderate dips are  
175 rather surprising for a strike fault zone and constitute a major structural element of F2 fault.

176 Several mechanisms may explain these unexpected fault dips. Post- faulting local or regional  
177 tilting may have later modified the fault attitude but can be excluded here because the bedding  
178 dip does not exceed 10° and because faults have no preferred inclination polarity, dipping  
179 either to the west or to the east. An alternative scenario is that F2 fault formed as a normal  
180 fault, with eventual flattening of the brittle planes due to compaction, and was later  
181 reactivated as a strike-slip fault. Following the paleostress reconstitution of Constantin et al.  
182 (2004) , the direction of extension during the Mesozoic rifting trended E-W and the direction  
183 of the Eocene compression switched from NE-SW to NW-SW direction. Such a stress  
184 succession would cause first normal slip, then dextral slip, and finally sinistral slip on F2

185 fault. Observations of these three types of fault movement in TF1 core suggests that F2 fault  
186 zone have suffered several periods of activities, in relation with the tectonic phases that  
187 affected the region during Meso-Cenozoic times. Alternative scenario, implying  
188 contemporaneous slips, is further developed in the discussion.

#### 189 4.2 Anisotropy of magnetic susceptibility

190 The anisotropy of magnetic susceptibility (AMS) can be represented as a second order  
191 symmetric tensor that can be represented geometrically as an ellipsoid with three principle  
192 susceptibility axes: maximum (K1), intermediate (K2) and minimum (K3) susceptibility with  
193 mean magnetic susceptibility  $K_m = (K_1 + K_2 + K_3) / 3$ . The AMS was estimated using a  
194 Geofyzika KLY-3 KappaBridge at the Paleomagnetism laboratory in the *Institut de Physique*  
195 *du Globe de Paris* (IPGP) (France).

196 The range of susceptibility values found in the Tournemire sediments are comprised between  
197  $135$  and  $200 \times 10^{-6}$  SI which suggests an important contribution of paramagnetic minerals  
198 (mainly clays). Thus, the AMS ellipsoids reflect mainly the preferred orientation of clay  
199 minerals, and can be used to investigate tectonic-related fabrics (Cifelli et al., 2009; Mattei et  
200 al., 1997; Parés et al., 1999). When normalized by the density (mass magnetic susceptibility),  
201 these values ranged between  $60$  and  $80 \times 10^{-9}$  m<sup>3</sup>/kg (Figure 5). We observed that, while in  
202 TF1 the susceptibility presented a normal distribution, a bimodal distribution was observed in  
203 ASM1. Mean values on the east (E) block of the fault were lower than in the west (W) block  
204 (Figure 5). The difference in magnetic susceptibility values between the east and west blocks  
205 could be related to the presence of calcite, a diamagnetic mineral. According to the  
206 mineralogical analyses carried out, the calcite content is higher in the eastern side.

207 Jelinek (1981) introduced different parameters to interpret the degree and shape of the  
208 anisotropy of magnetic susceptibility: lineation ( $L=K1/K2$ ); foliation ( $F=K2/K3$ ). The shape  
209 parameter ( $T$ ) combines the lineation and foliation parameters ( $T = ((\ln L - \ln F)/(\ln L + \ln$   
210  $F))$ ). Positive  $T$ -values imply an oblate ellipsoid, negative values imply prolate ellipsoid, and  
211  $T$ -values close to zero imply neutral ellipsoids. Finally,  $P_j$  is the corrected degree of  
212 anisotropy ( $P_j = \exp(\sqrt{2[(\ln(K1/km))^2 + \ln(K2/km)^2 + \ln(K3/km)^2]})$ ). Higher  $P_j$  values imply  
213 increasing strength of the ellipsoid shape.

214 The evolution of magnetic fabric along the cores was inferred by the Jelinek diagram ( $T$   
215 versus  $P_j$ ) (Figure 5) and by the equal-area, lower-hemisphere projection of the  $K1$  and  $K3$   
216 axes using the Anisoft software (Figure 6). A bedding plane dip of  $10^\circ$  towards the north is  
217 reported that corresponds to the measurements estimated by Dick et al. (2016) in the  
218 undamaged and damage zone at the west side of the fault.

219 With the increasing tectonic deformation, the evolution of the magnetic fabric can follow  
220 different stages (Borradaile and Henry, 1997; Parés et al. 1999; Parés 2004, 2015): The type I  
221 corresponds to the sedimentary fabric and is characterized by the  $K3$  axes perpendicular and  
222 the  $K1$  axes are distributed on the bedding plane without a predominant magnetic lineation.  
223 The  $P_j$ - $T$  diagrams show magnetic fabrics characterized by strongly oblate shaped  
224 susceptibility ellipsoids. If the sediments are deposited under a weak current flow, the  $K1$   
225 axes can be aligned parallel to the paleocurrent flow azimuth.

226 Type II corresponds to a weak-moderate deformation with the  $K3$  axes perpendicular to the  
227 bedding plane and the  $K3$  axes parallel to the extensional direction. Type III, corresponding  
228 to a high deformation stage. The  $K3$  axes show a girdle that is parallel to the maximum  
229 shortening direction and the  $K1$  axes perpendicular to it. Furthermore, the  $P_j$ - $T$  diagrams

230 show a neutral ellipsoid that could be developed due to tectonic compression. The last stage  
231 of deformation (type IV) is reached when K3 is within the bedding plane and the ellipsoid is  
232 prolate.

233 In the undamaged zone of core TF1, the AMS ellipsoid had a predominantly oblate shape  
234 with a magnetic foliation parallel to the bedding plane (Figure 6). The shape of AMS  
235 ellipsoid at this zone had a generally oblate shape with a low degree of anisotropy (Figure 5)  
236 and the maximum axes are relatively well clustered with a general NE–SW orientation. An  
237 oblate fabric was also observed in the damage zone. In this case the K1 axes are rotated in  
238 anti-clockwise direction. and the minimum K3 axis had a lower inclination values (75-80°)  
239 that can be explained by the observed increase in bedding plane dip towards the fault core  
240 (Dick et al. 2016). Within the fault core, the AMS ellipsoids had very different signatures in  
241 sections 1353-1380 cm (west side) and 1406-1432 cm sections (east side). In section 1353-  
242 1406 cm, we can observe a type III fabric, the minimum K3 axes are distributed around a  
243 girdle from the vertical to the horizontal plane and the maximum K1 axes follows a NW-SE  
244 orientation. In addition, the Jelinek diagram (Figure 5) shows a strong decrease of the  
245 anisotropy degree (P) and a change of the magnetic shape factor (T) from high oblate (T~1)  
246 to neutral (T~0).

247 The samples from section 1406-1432 section revealed also a girdle distribution of the K3  
248 axes but the K1 axes follow a NE-SW direction. The Jelinek diagram indicates an oblate  
249 fabric.

250 Conversely, in ASM1, the magnetic fabric was very similar in the damage and the fault core.  
251 It was characterized by an inclination of the K3 axes of 75-80° and an orientation of the K1  
252 axes towards a NW-SE direction (Figure 6). We didn't observe the developpement of a type

253 III fabric but the Jelinek diagram (Figure 5) shows a slight decrease in T from 1 to moderate  
254 values ( $T \sim 0.5$ ) indicating a weak deformation stage. In addition, we also observed higher  
255 degree of anisotropy ( $P_j$ ) at the E-block. This part of the fault is also characterized by lower  
256 magnetic susceptibility (Figure 5 and Figure 7).

#### 257 4.3 Anisotropy of P-wave velocity

258 The P-wave velocity ( $V_p$ ) was measured on the cubes from both cores TF1 and ASM1 along  
259 the three axes x, y and z using ultrasonic transducers with dominant frequency 1 MHz, a  
260 Panametrics 5058 PR pulser and a digital oscilloscope. The velocity is conventionally  
261 inferred from the travel time for a wave propagating from the transmitter to the receiver.  
262 Previous works showed that compressional wave velocity is inversely correlated to total  
263 porosity and clay mineral contents (Han et al., 1986). In addition, in normal consolidated  
264 sediments, the Pwave velocity is faster in the bedding plane than perpendicular to it.

265 The anisotropy of P-wave velocity (APV) is defined as the difference between maximum and  
266 minimum velocities normalized to the average velocity:

267  $APV(\%) = 100 * (V_p \text{ max} - V_p \text{ min}) / V_p \text{ mean}$ , where  $V_{pmin}$  is the P-wave velocity in the Z  
268 direction ( $V_{pz}$ ), perpendicular to bedding, and  $V_{pmean}$  the average velocity in the bedding  
269 plane  $(V_{px} + V_{py}) / 2$ . The  $V_p \text{ mean}$ ,  $V_{pz}$  and the APV (%) are shown in Figure 7. The P-wave  
270 velocities in the bedding plane were much higher than the vertical one and lead to large APV  
271 values of around 50% in the undeformed zone to around 40% in the damage zone. In core  
272 TF1, we observed a drastic change within the fault core with a strong dispersion of APV  
273 values down to negative values, reflecting elastic anisotropy reversal. This is mainly due to  
274 the increase in P-wave velocity along the vertical axis and a decrease in the horizontal axes.  
275 Such a change is not observed in the fault core of ASM1. We can observe that in general the

276 changes in the P-wave velocity and the APV are in phase with changes the AMS properties  
277 (Figure 7).

#### 278 4.4 Clay minerals assemblages and bulk mineralogy

279 Bulk mineralogy and clay mineral assemblages were identified using X-ray diffraction  
280 (XRD). It should be remembered that the samples for the XRD and MEB measurements  
281 come from a block of total sediment in the undamaged zone and from the first millimetres  
282 along the slip planes from fractures in the damage zone and in the fault core.  
283 XRD samples were prepared according to the powder diffraction method (Brindley and  
284 Brown, 1980). For clay mineral preparation, we followed the analytical procedure of  
285 Holtzapffel (1985). X-ray diffractograms were obtained using a D2 Bruker diffractometer  
286 equipped with a Lynx Eye detector, with  $\text{CuK}\alpha$  radiation and NI filter. Measurement  
287 parameters were as follows: 2.5 to 35° (2 $\theta$ ), in steps of 0.02° each 0.2 s. The identification of  
288 clay minerals was made according to the position of the (001) reflections of the X-ray  
289 diffractograms (Brindley and Brown, 1980; Moore and Reynolds, 1989) using a MacDiff  
290 software.

291 XRD analysis was complemented by the analysis of some bulk samples from the undamaged  
292 host rock and fractures planes within the damage zone in a scanning electron microscopy  
293 coupled to an energy-dispersive X-ray spectrometry system (SEM-EDS). We used a ZEISS  
294 supra V5 instrument provided with a BRUKER detector in energy dispersive spectroscopy  
295 (EDS) at the Petrology, Geochemistry, Magmatic Mineralogy Laboratory (PG2M) ISTEP of  
296 the University Pierre and Marie Curie (Paris).

297 The major mineral assemblages identified by XRD analysis were clays (18-48%, mean  
298 37%), quartz (21-48%, mean 37%) and calcite (9-61%; mean 27%). Pyrite and siderite were  
299 found as secondary minerals with concentrations below 5% and they were not quantified. We

300 observed small quantities of ankerite and ferroan dolomite both in the undeformed host rock  
301 sediment and in the damage zone by SEM-EDS (Figure 9). This finding is in agreement with  
302 previous studies (Lerouge et al., 2012; Peyaud et al., 2006). We must note that core TF1 was  
303 drilled in 1999 and that some mineralogical alteration could have occurred. However, its  
304 composition is similar to the one in core ASM1, collected 14 years later indicating that post-  
305 drilling alteration didn't change the original mineralogical composition.

306 The calcite content in the western undamaged zone is very low (~15%) (Figure 8) and  
307 corresponds to the average calcite content estimated in the Tournemire site (Boisson et al.  
308 1996). As we approach the centre of the fault, the calcite content from slip planes showed  
309 very scattered values (10-60% in core TF1 and 9-51% in core ASM1) indicating that some  
310 fractures are filled with calcite cement and some other are not. This calcification took place  
311 during two episodes of compressive deformation during the Pyrenean orogeny (Lefèvre et al.,  
312 2016).

313 Additionally, we also observed higher CaCO<sub>3</sub> content in the eastern compartment (30-35%)  
314 (end of damage zone and undeformed zone), reaching 30-35% (Figure 8). We interpret that  
315 this increase is not caused by precipitations from tectonically induced fluids  
316 (macroscopically, we found no veins in this core section/ these samples) but that it rather  
317 indicates a different background signature for calcite content eastwards of the fault zone.

318 Average proportions of the various clay species in TF1 and ASM1 cores are very similar  
319 (Figure 8). The clay mineral assemblage in core TF1 consisted of illite (35 to 45%, near 40%  
320 on average), kaolinite (25 to 40%, 33% on average), illite-smectite mixed layers  
321 (I/S, 15 to 25%, 19% in average) and chlorite (5 to 10%, 9% in average).

322 The clay mineral assemblage in core ASM1 consisted of illite (5 to 40%, 36% on average),  
323 kaolinite (30 to around 40%, 34% on average), I-S (15 to 35%, 21% on average) and chlorite  
324 (5 to 10%, 9% on average).

325 Clay mineral proportions in TF1 and ASM1 cores were also very similar to the ones  
326 previously determined at Tournemire site (Savoie et al.,2008; Dick et al. 2016). However,  
327 while Savoie et al. (2008) didn't show any significant change in the clay assemblage as  
328 function of the distance to the fault plane, our results revealed a weak but noticeable increase  
329 in kaolinite (Figure 8). The maximal difference in kaolinite content between the undamaged  
330 and the fault core zones is 14% in core ASM1 and 9%, in core TF1, slightly higher than the  
331 analytical error ( $\pm 5\%$ ). We interpret this mineralogical evolution as significant as the same  
332 mineralogical trend is observed in both ASM1 and TF1 cores toward the deformed zones. A  
333 previous work indicates that the proportion of kaolinite, can be even higher (63-72%) when  
334 we look at the fault gouge (Dick et al. 2016). Such a kaolinite increase toward the fault core  
335 has been considered to reflect a high degree of fluid-rock interaction (Rossetti et al. 2010).

336 An additional mineralogical change recorded in our data set ASM1 (Figure 8) is  
337 characterized by a large increase in I/S proportions correlated with a decrease in illite from  
338 the fault core boundary (I/S 16% and illite 42%) to the eastern undamaged zone (I/S 35% and  
339 illite 23%). This sharp mineralogical change may suggest a vertical offset that can be more  
340 important in ASM1. After the difference in the dolomitic horizon marker observed on either  
341 side of the fault, suggest that the amount of the perpendicular slip is of around 4–6 m (Dick et  
342 al. 2016).

#### 343 4.5 Magnetic mineralogy based on low temperature SIRM

344 Low-temperature isothermal remanence magnetizations (LT-SIRM) were made in core TF1  
345 using a Quantum Design Magnetic Property Measurement System (MPMS2) SQUID



346 magnetometer at the IPGP Paleomagnetic laboratory in Paris (France). The powders used for  
347 these analysis were collected on the fault planes and fractures at different points of core TF1  
348 with the exception of the sample in the undeformed zone which comes from the bulk  
349 sediment.

350 Two different LT-SIRM experiments were performed. First, samples were cooled in zero  
351 field to 10 K, and a magnetic field of 2.5T was given at 10 K. The SIRM was measured in  
352 approximately zero field at 5-K intervals up to 300 K (zero-field cool curves, ZFC). In the  
353 second experiment, the samples were cooled in a high magnetic field of 2.5 T and then the  
354 SIRM was measured again every 5K up to 300 K (field-cool curves, FC).

355 We observed two transitions in the ZFC and FC curves: A small drop at 120 K, in the  
356 majority of the samples (sometimes only observed in the first derivate curves) which  
357 corresponds to temperature of the magnetite Verwey transition,  $T_v$  (Verwey, 1939) (Figure  
358 10). The elevation of FC SIRM over ZFC SIRM and the small loss in remanence across the  
359  $T_v$  warming indicates a very fine grain-size, lower than  $0.1\mu\text{m}$  which correspond to single-  
360 domain (SD) magnetite (Özdemir et al., 2002; Smirnov, 2009). In addition, a linear decrease  
361 trend observed in the FC and ZFC SIRM curves above the Verwey transition ( $T > 120\text{ K}$ )  
362 indicates the presence of superparamagnetic (SP) grains. The frontier between the SP and SD  
363 grains depends on the shape of magnetite but for detrital magnetite with isotropic grains, the  
364 limit is at around  $0.017\mu\text{m}$  (Muxworthy and Williams, 2009).

365 In addition, magnetite is characterized to have a high remanence at room temperature and we  
366 used the SIRM at 300K ( $\text{SIRM}_{300\text{K}}$ ) to evaluate the evolution of magnetite content along the  
367 TF1.

368 A second large drop in remanence was observed around 35K and it was related to the Neel  
369 transition of siderite. Siderite is also characterized by a FC remanence below 40K much  
370 larger than the ZFC remanence (Housen et al. 1996).

371 Two other minerals have magnetic transitions around 35K: rhodochrosite ( $\text{MnCO}_3$ ) whose  
372 Neel temperature is 32K (Housen et al., 1996) and pyrrhotite ( $\text{Fe}_{1-x}\text{S}$ ) which has a magnetic  
373 transition at 35 K (Dekkers et al., 1989; Rochette et al., 1990) now known as Benus transition  
374 (Rochette et al., 2011). Aubourg and Pozzi (2010) as well as Aubourg et al. (2008) attributed  
375 the drop in the ZFC/FC curves in samples from Mont Terri Lower Dogger claystones to a  
376 combination of paramagnetic input (clay minerals), pyrrhotite transition and the effect of  
377 superparamagnetic grains (SP). However, in Tournemire site, pyrrhotite wasn't found neither  
378 by XRD analysis nor SEM/EDS observations while siderite can be detected by XRD and  
379 have concentrations lower than 5%.

380 The magnetic mineralogy evolution from the undeformed host rock to the fault core was  
381 studied using the  $\text{SIRM}_{300\text{K}}$  used as an estimate of fine-grained magnetite and FC/ZFC ratio  
382 at 10 K, used to indicate the occurrence of siderite. For pure siderite, the difference is higher  
383 than 10 (Frederichs et al., 2003; Housen et al., 1996).

384 We observed a sharp increase in the  $\text{SIRM}_{300\text{K}}$  values in the damage zone (Figure 10) in  
385 phase with a decrease in the FC/ZFC<sub>10K</sub> ratio. These changes were interpreted as a partial  
386 oxidation of siderite to magnetite due to the presence of fluid circulations (Ellwood et al.,  
387 1986).

## 388 **5. Discussion**

389 The multi-proxies approach used in this study confirmed the commonly accepted zooning  
390 along a fault zone: an undamaged area characterized by samples with little or no fracturing, a

391 damage zone with a large number of calcified fractures and a fault core characterized by high  
392 deformation and no apparent bedding. Based on this finding, it is tempting to assume a fault  
393 zone evolution where a tectonic rework of the host rock lead to the formation of gouge,  
394 which we assume to accommodate the largest part of the faults' offset (Dick et al., 2016,  
395 Laurich et al. 2018).

396 Our work indicates three main findings:

- 397 - The tectonic analysis of fractures indicated that the F2 fault underwent a polyphased  
398 evolution with reactivations under different tectonic regimes. Two strike-slip regimes,  
399 with approximate NE-SW and NW-SE compression, and a normal regime with a WNW-  
400 ESE direction of extension are inferred from the orientation of the fault-slips. Most of the  
401 N-S fault planes collected in TF1 core, whatever their movement, show dip values  
402 between 5° to 45°. This finding constitutes a major structural characteristic of F2 fault.
- 403 - Second, our study demonstrated that the anisotropy of P-wave velocity (APV) and of  
404 susceptibility (AMS) follows the fault zoning in agreement with the results obtained by  
405 Bonnelye (2016). We observed the loss of the primary sedimentary fabric in the damage  
406 zone and an important decrease in the anisotropy of magnetic susceptibility (AMS) and  
407 the P-wave velocity (APV) within the fault core, especially in TF1 core.
- 408 - Third, we identified evidence of neo-formation of fine-grained magnetite (only measured  
409 in core TF1), precipitation of millimetric to infra-millimetric calcite veins and a potential  
410 neoformation of kaolinite within the fault planes in the damage and the core fault.

#### 411 5.1 Polyphased fault zone development

412 Fault data collected along the F2 fault evidenced the complex nature of the damage zones of  
413 this fault. The damage zones include individual fractures with horizontal and dip slip

414 movements, sometimes in opposite directions. The NS+- 20 sinistral slip surfaces observed in  
415 this study are in agreement with a left lateral movement observed on other segments of F2  
416 fault in the Tournemire URL (Constantin et al., 2002; Lefèvre et al., 2016).

417 Sinistral and reverse faults in TF1 both indicate a local N130°E  $\sigma_H$  (maximal horizontal  
418 stress) and a N040°E  $\sigma_h$  (minimal horizontal stress), in agreement with the N130°E  
419 compression inferred from fault-slip data inversion close to the northern continuation of F2 in  
420 the western gallery (Constantin et al., 2002). Dextral faults result from a N45°E  $\sigma_H$  and  
421 N135°E  $\sigma_h$ . A rather similar WNW-ESE  $\sigma_h$  is inferred from the normal faults and is  
422 associated with a normal stress regime.

423 We propose two different scenarios that may explain this tectonic complexity (Figure 11). We  
424 consider (1) a long lived scenario, with fault activity starting in Mesozoic time and regional  
425 stresses changing through time (Figure 11A), and (2) a short scenario, in which the fault  
426 internal architecture evolved progressively during the displacement accumulation (Figure  
427 11B). Scenarios between these two end member models may further exist. In scenario 1  
428 (Figure 11A), the F2 fault initiated as a normal fault during Mesozoic time under a WNW-  
429 ESE extension. As such an extension regime is active during the Toarcian (Constantin et al.,  
430 2002), normal faults in Tournemire may predated sedimentary compaction. Subsequent, the  
431 F2 fault registered a first dextral slip and a later sinistral one in Eocene time during the  
432 Pyrenean orogeny. These two opposite slips result from the counter clockwise stress rotation  
433 of the Pyrenean compression, from a N20°E to a N160°E direction (Constantin et al., 2002).  
434 In scenario 2 (Figure 11B), the F2 fault observed in the gallery section is a linking fault in an  
435 extensive relay between two NNW-SSE dextral faults formed during the Pyrenean orogeny.  
436 The normal faults recognized in the TF1 core formed when these two dextral segments were  
437 linked (Figure 11B1). Such a development is confirmed in analogue models (Rahe et al.,

438 1998). In the latest stage, the strike-slip fault cut the relay (Figure 11B2) and formed the F2  
439 fault. The relay zone was later reactivated as a sinistral strike-slip fault in response to the  
440 counter clockwise rotation of the Pyrenean compression (Figure 11B3).

441 Both scenarios are in agreement with the sinistral reactivation of previously dextral faults  
442 observed by Lefevre et al. (2016) along another section of F2 fault. Interestingly, the earlier  
443 dextral slips are more preserved in the studied portion of the fault zone (50% of the measured  
444 fault surfaces in TF1 core). The left lateral reactivation of the fault requires that N160°E  
445 compression was deflected close to the fault in order to have a sufficient shear stress.  
446 Accordingly, the local stress tensor obtained by Constantin et al. (2002) in the Tournemire  
447 gallery indicates that the compression adopted here a N130°E strike.

#### 448 5.2 Fault zoning and longitudinal heterogeneity of anisotropy of p-wave velocity and 449 magnetics susceptibility

450 We found an excellent correlation between the anisotropy of magnetic susceptibility (AMS)  
451 and the P-wave velocity (APV) in cores TF1 and ASM1. In the case of argillites, the  
452 susceptibility and P-wave velocity are mainly controlled by the preferred orientation of the  
453 clay sheets and explains while the magnetic and elastic results converge (David et al., 2007).

454 The results of AMS in ASM1 and TF1 cores indicate that there is a dominance of type II and  
455 type III fabrics with oblate to neutral ellipsoids. A magnetic lineation trending NW-SE was  
456 observed in the damage zone and in majority of the samples of the fault core zones. Following  
457 Mattei et al. (1997) and Parés (2004), this magnetic lineation is usually developed parallel to  
458 the extension direction. The observed K1 preferred orientation can result from strike-slip  
459 regime with  $\sigma_1$  trending NE-SW. Such stress state is in agreement with the numerous dextral  
460 slip measured in the fault zone. The AMS fabric was thus acquired during the dextral

461 movement along F2 fault during the Pyrenean orogeny. The normal movement, whatever their  
462 age, may also have produced the magnetic fabric, but its contribution is thought to have been  
463 less important.

464 Interestingly, the magnetic fabric in section 1402-1432 in the TF1 core showed a different  
465 pattern. In this case, the K3 axes formed a girdle in the NW-SE direction and the K1 axes  
466 were preferably oriented in the NE-SW direction. Several mechanisms could explain this  
467 change. It could indicate that the eastern side of the fault imprints the deformation due to  
468 sinistral reactivation of previously dextral faults. This fabric was also observed in this  
469 section. It would be necessary to study other parts of the fault to affirm or decline this  
470 hypothesis. On the other hand, AMS tectonic fabric is very sensitive to localized deformation  
471 zones such as gouge or deformation bands that are very abundant in this part of the fault. The  
472 impact of these deformations on the AMS fabric is an issue that needs to be further explored  
473 (Parés, 2015).

474 Similarly, a complete reversal of elastic anisotropy ( $APV < 0$ ) was also observed within the  
475 fault core. Recent experiments on Tournemire shale (Bonnelye et al., 2017) and creep tests  
476 (Geng et al., 2017) show an inversion of elastic anisotropy in samples deformed  
477 perpendicularly to bed changes due to mineral rotation near fault zones. A tectonic fabric is  
478 also detected in a borehole from the Mont Terri rock laboratory thanks to a decrease in the p-  
479 wave velocity (Jaeggi et al., 2017).

480 Thus, the petrophysical results observed within the fault core of TF1 were interpreted as the  
481 result of an intense damage process. Here, the bed is only preserved in centimetre -thick  
482 zones (Lefevre et al. 2016) which may explain why the % APV and K3 axes showed such

483 scattered values (Figure 7), these parameters being particularly sensitive to bedding  
484 orientation.

485 Another important result is that the preferred orientation of the K1 axes in the undamaged  
486 zone (only available in TF1) was in the NE-SW direction. One possible mechanism is that the  
487 alignment of the K1 axes in the undamaged zone is due to a deposition under the influence of  
488 a bottom current. In this case, the direction of the K3 axes is perpendicular to the bedding  
489 plane and the K1 axes are parallel to the current direction (Beckers et al. 2016; Singsoupho et  
490 al. 2015; Parès et al. 2007). Further studies will be necessary to confirm this hypothesis.

491 In ASM1, the AMS and elastic anisotropy didn't show such drastic changes in the fault core.  
492 The AMS analysis indicated a type II tectonic fabric (Parès, 2015) and a slight decrease in  
493 the p-wave velocity at 300 cm within the fault core. In the fault core, the sediment is  
494 characterized by small deformed volumes, shear zones, shear bands and gouge intercalated  
495 with apparently undeformed sediment (Laurich et al. 2017; Dick et al. 2016; Lefevre et al.  
496 2016). Despite the care we took in the sampling procedure, the number of sampled cubes  
497 were limited by the large number of fractures and it cannot be totally ruled out that the  
498 deformation of these relatively small volumes zones were less reflected in ASM1 because  
499 they couldn't be sampled. The magnetic fabric in the damage and the fault core in ASM1  
500 show however a similar a preferred orientation of the K1 axes in the NW-SE direction in  
501 agreement with the dextral strike-slip regime.

502 Finally, one of the major characteristic found in core ASM1 was the dissymmetry observed  
503 in P-wave velocity, magnetic susceptibility and  $P_j$  between the western and eastern parts of  
504 the fault. The observed differences seem to be related to a mineralogical change and not to  
505 strain and they were not observed in TF1. Mineralogical analysis indicates higher calcite

506 content in the eastern side and an increase in illite-smectite mixed layers towards the east. As  
507 the core was drilled horizontal to the bedding plane, the stratigraphic level (and therefore the  
508 mineralogical composition), should be the same on both sides of the fault, unless there is a  
509 vertical offset. This vertical offset was observed by Dick et al. (2016). We cannot however  
510 quantify it.

### 511 5.3 Fluid circulation in the fault zone

512 The XRD analyses showed evidence of precipitation of millimetric to infra-millimetric calcite  
513 veins and a potential neoformation of kaolinite along the fault planes in the damage zone/fault  
514 core zones. This was already observed in a previous study of Tournemire shales which  
515 indicated that maximum kaolinite content was observed in the fault gouge (Dick et al., 2016).

516 The increase of kaolinite abundance towards the fault core suggests a high degree of fluid–  
517 rock interaction (Rossetti et al., 2011).

518 In addition, the LT-SIRM measurements enabled the identification of small amount of siderite  
519 in our samples. Siderite was also identified by XRD but it was not quantified by XRD  
520 because its concentration was less than 5%. However, magnetic measurements like SIRM are  
521 able to detect ferrimagnetic minerals that are undetected by traditional mineralogical analyses  
522 such as XRD, even when the concentrations are as low as 1 ppm (Lagroix, F. and Y. Guyodo,  
523 2017).

524 Besides, the SIRM<sub>300k</sub> and FC/ZRC record indicated an increase in fine-grained magnetite and  
525 a decrease in siderite towards the damage/fault core boundary (Figure 9).

526 In Tournemire shales, the fluid circulation mainly occurs between the fault core and the  
527 damage zone (Guglielmi et al., 2015; Lefèvre et al., 2016) in which the porosity reaches  
528 maximum values (Dick et al., 2016). Therefore, the transformation of siderite into magnetite



529 seems to be a good index of paleo-fluid circulation and indicates a change in redox conditions  
530 related with episodic connections with less reduced fluids from the overlying aquifer (Peyaud  
531 et al., 2006). We suggest however the prevalence of reducing conditions, as at higher  
532 oxidation rates, the final product of siderite will be hematite instead of magnetite (Ellwood et  
533 al., 1986). The presence of minerals like ankerite, calcite, ferroan dolomite and framboidal  
534 pyrite observed in the SEM (Figure 8) supports also the prevalence of reducing conditions and  
535 were also observed by Peyaud et al. (2006) and Lefèvre et al. (2016).

## 536 **6. Conclusions**

537 The integrated study of the N-S F2 fault cutting the Toarcian shale formation from the  
538 Tournemire Underground Research Laboratory (URL) made it possible to highlight the  
539 existing relationships between the fault architecture and its tectonic history with the variations  
540 of petrophysical properties (anisotropy of magnetic susceptibility and P-wave velocity) and  
541 mineralogy (CaCO<sub>3</sub>, clays and magnetic mineralogy).

542 The fault surfaces within the fault zone pointed out that the F2 fault suffered a polyphased  
543 tectonic history, with successive reactivations under normal and strike-slip regimes. Notably,  
544 slips on fault surface within the damage zone occurred mostly on shallow or very shallow (5°  
545 to 45°) dipping N-S fault planes.

546 Our study demonstrated that the anisotropy of P-wave velocity (APV) and of susceptibility  
547 (AMS) are well correlated and they follow the fault zoning. In the damage zone, changes in  
548 the ASM and APV properties were mainly related to an increase in the bedding plane dip.

549 Within the fault core zone, a strong anisotropy reversal was observed which indicated a strong  
550 sediment deformation and suggest clay platelets rotation near failure. These deformations are  
551 however located in very small volumes (deformed bands and gouge).

552 The observed NW-SE magnetic lineation in both cores ASM1 and TF1 was acquired during  
553 the first dextral slip during the Pyrenean orogeny.  
554 The magnetite and potential kaolinite neoformation attest of fluid circulation at the vicinity of  
555 the damage/fault core boundary and suggest that the transformation of siderite in magnetite  
556 may be a good index of paleo-fluid circulation.  
557 The variability of the response observed in the two studied cores suggests the need to study  
558 the characteristics of the fault both across its different architectural zones and along the main  
559 fracture plan.

#### 560 **Acknowledgment**

561 This work was funded by a collaboration contract between the IRSN, the CNRS and the  
562 MNHN (number DAF CJ/SL/BL-11831). We are grateful to France Lagroix for allowing us  
563 the access to the Paleomagnetism laboratory of the IPGP for the susceptibility measurements  
564 and for her support given during the low-T SIRM measurements. We are grateful and to  
565 Omar Boudouma for his support given during the SEM sessions and for Frederic Delbès in  
566 helping for clay mineral analyses. We thank Ben Laurich and the anonymous reviewer for  
567 their constructive criticism of the paper.

568

569 **References**

570

571 Aubourg, C., Pozzi, J.-P., 2010. Toward a new < 250 °C pyrrhotite–magnetite  
572 geothermometer for claystones. *Earth and Planetary Science Letters* 294, 47-57.

573 Aubourg, C., Pozzi, J.P., Janots, D., Sahraoui, L., 2008. Imprinting chemical remanent  
574 magnetization in claystones at 95 °C. *Earth and Planetary Science Letters* 272, 172-180.

575 Beckers, A., C. Beck, A. Hubert-Ferrari, E. Tripsanas, C. Crouzet, D. Sakellariou, G.  
576 Papatheodorou and M. De Batist, 2016. Influence of bottom currents on the sedimentary  
577 processes at the western tip of the Gulf of Corinth, Greece. *Marine Geology* 378: 312-332.

578 Boisson J-Y., Cabrera J. and D. W. L. (1996). Caractérisation des propriétés de transferts au  
579 laboratoire des argilites et marnes toarciennes de Tournemire, IRSN report.

580 Bonnelye, A., 2016. Etude des propriétés physiques et mécaniques des argilites : de la  
581 déformation en laboratoire aux failles naturelles. Thèse de doctorat en Sciences de la terre et  
582 de l'univers. Université de Cergy-Pontoise.

583 Bonnelye, A., Schubnel, A., David, C., Henry, P., Guglielmi, Y., Gout, C., Fauchille, A.L. and  
584 Dick, P., 2017. Elastic wave velocity evolution of shales deformed under uppermost-crustal  
585 conditions, *Journal of Geophysical Research.*, 122, 130-141.

586 Borradaile, G.J., Henry, B., 1997. Tectonic applications of magnetic susceptibility and its  
587 anisotropy. *Earth-Science Reviews* 42, 49-93.

588 Bretaudeau, F., Gélis, C., Leparoux, D., Brossier, R., Cabrera, J., Côte, P., 2014. High-  
589 resolution quantitative seismic imaging of a strike-slip fault with small vertical offset in clay  
590 rocks from underground galleries: Experimental platform of Tournemire, France. *Geophysics*  
591 79, B1-B18.

592 Brindley G.W., Brown G., 1980. Crystal structures of clay minerals and their X-ray  
593 identification. Mineralogical Society - London.

594 Cabrera, J., P. Volant, C. Baker, W. Pettitt and R. P. Young, 1999. Structural and geophysical  
595 investigations of the EDZ (Excavation Disturbed Zone) in indurated argillaceous media: The  
596 tunnel and the galleries of the IPSN Tournemire site, France, *American Rock Mechanics*  
597 Association.

598 Cabrera, J., 2002. Caractérisation des discontinuités en milieu argileux (station expérimentale  
599 de Tournemire). Questions clés relatives à l'évaluation de la sûreté du stockage des déchets  
600 radioactifs, Rapport scientifique et technique. Institut De Radioprotection et de Sûreté  
601 Nucléaire, pp. 227-232.

602 Cifelli, F., Mattei, M., Chadima, M., Lenser, S., Hirt, A.M., 2009. The magnetic fabric in  
603 “undeformed clays”: AMS and neutron texture analyses from the Rif Chain (Morocco).  
604 *Tectonophysics* 466, 79-88.

- 605 Constantin, J., Vergély, P., Cabrera, J., 2002. Tectonic evolution and related fracturing in the  
606 Causses Basin (Aveyron, France) : the Tournemire area example. *Bulletin de la Societe*  
607 *Geologique de France* 173, 229-243.
- 608 Constantin, J., Peyaud, J.B., Vergély, P., Pagel, M., Cabrera, J., 2004. Evolution of the  
609 structural fault permeability in argillaceous rocks in a polyphased tectonic context. *Physics*  
610 *and Chemistry of the Earth, Parts A/B/C* 29, 25-41.
- 611 David, C., Robion, P., Menéndez, B., 2007. Anisotropy of elastic, magnetic and  
612 microstructural properties of the Callovo-Oxfordian argillite. *Physics and Chemistry of the*  
613 *Earth, Parts A/B/C* 32, 145-153.
- 614 De Barros Louis, Daniel Guillaume, Guglielmi Yves, Rivet Diane, Caron Hervé, Payre  
615 Xavier, Bergery Guillaume, Henry Pierre, Castilla Raymi, Dick Pierre, Barbieri Ernesto and  
616 G. Maxime, 2016. Fault structure, stress, or pressure control of the seismicity in shale?  
617 Insights from a controlled experiment of fluid- induced fault reactivation. *Journal of*  
618 *Geophysical Research: Solid Earth* 121(6): 4506-4522.
- 619 Dekkers, M.J., Mattéi, J.L., Fillion, G., Rochette, P., 1989. Grain-size dependence of the  
620 magnetic behavior of pyrrhotite during its low-temperature transition at 34 K. *Geophysical*  
621 *Research Letters* 16, 855-858.
- 622 Dick, P., Wittebroodt, C., Courbet, C., Rvi, J.S., Estève, I., Matray, J.-M., Siitari-Kauppi, M.,  
623 Voutilainen, M., Dauzères, A., 2016. The internal architecture and permeability structures of  
624 faults in shale formations. *The Clay Minerals Society Workshop Lectures Series* 21, 219-229.
- 625 Ellwood, B.B., Balsam, W., Burkart, B., Long, G.J., Buhl, M.L., 1986. Anomalous magnetic  
626 properties in rocks containing the mineral siderite: Paleomagnetic implications. *Journal of*  
627 *Geophysical Research: Solid Earth* 91, 12779-12790.
- 628 Faulkner, D. R., C. A. L. Jackson, R. J. Lunn, R. W. Schlische, Z. K. Shipton, C. A. J.  
629 Wibberley and M. O. Withjack, 2010. A review of recent developments concerning the  
630 structure, mechanics and fluid flow properties of fault zones. *Journal of Structural Geology*  
631 32(11): 1557-1575.
- 632 Frederichs, T., von Dobeneck, T., Bleil, U., Dekkers, M.J., 2003. Towards the identification  
633 of siderite, rhodochrosite, and vivianite in sediments by their low-temperature magnetic  
634 properties. *Physics and Chemistry of the Earth, Parts A/B/C* 28, 669-679.
- 635 Geng, Z., Bonnelye, A., Chen, M., Jin, Y., Dick, P., David, C. and Schubnel, A., 2017. Elastic  
636 anisotropy reversal during brittle creep in shale, *Geophys. Res. Lett.*, 44, 121, 10887-10895.
- 637 Guglielmi, Y., Elsworth, D., Cappa, F., Henry, P., Gout, C., Dick, P., Durand, J., 2015. In situ  
638 observations on the coupling between hydraulic diffusivity and displacements during fault  
639 reactivation in shales. *Journal of Geophysical Research: Solid Earth* 120, 7729-7748.
- 640 Han, D.-h., Nur, A., Morgan, D., 1986. Effects of porosity and clay content on wave  
641 velocities in sandstones. *Geophysics* 51, 2093-2107.

- 642 Housen, B.A., Banerjee, S.K., Moskowitz, B.M., 1996. Low-temperature magnetic properties  
643 of siderite and magnetite in marine sediments. *Geophysical Research Letters* 23, 2843-2846.
- 644 Holtzapffel, T. (1985). Les minéraux argileux : préparation, analyse diffractométrique et  
645 détermination. *Société Géologique du Nord* 12, 1543.
- 646 Jaeggi, D., Laurich, B., Nussbaum, C., Schuster, K., & Connolly, P. 2017. Tectonic structure  
647 of the “Main Fault” in the Opalinus Clay, Mont Terri rock laboratory (Switzerland). *Swiss*  
648 *Journal of Geosciences*, 110(1), 67–84. <https://doi.org/10.1007/s00015-016-0243-2>.
- 649 Jelinek, V. (1981). Characterization of the magnetic fabric of rocks. *Tectonophysics* 79: 63-  
650 67.
- 651 Lagroix, F. and Y. Guyodo, 2017. A New Tool for Separating the Magnetic Mineralogy of  
652 Complex Mineral Assemblages from Low Temperature Magnetic Behavior. *Frontiers in Earth*  
653 *Science* 5(61).
- 654 Laurich, B., Urai, J. L., Vollmer, C., and Nussbaum, C., 2018. Deformation mechanisms and  
655 evolution of the microstructure of gouge in the Main Fault in Opalinus Clay in the Mont Terri  
656 rock laboratory (CH), *Solid Earth*, 9, 1-24, <https://doi.org/10.5194/se-9-1-2018>.
- 657 Lefèvre, M., Guglielmi, Y., Henry, P., Dick, P., Gout, C., 2016. Calcite veins as an indicator  
658 of fracture dilatancy and connectivity during strike-slip faulting in Toarcian shale  
659 (Tournemire tunnel, Southern France). *Journal of Structural Geology* 83, 73-84.
- 660 Lerouge, C., Grangeon, S., Fléhoc, C., Buschaert, S., Mazurek, M., Matray, J.-M., Tournassat,  
661 C., 2012. Diagenetic carbonates in clay-rich marine formations, International meeting "Clays  
662 in Natural and Engineered Barriers for Radioactive Waste Confinement", Montpellier, France.
- 663 Louis, L., T.-M. Natalie Chen, C. David, P. Robion, T.-f. Wong and S.-r. Song, 2008.  
664 Anisotropy of magnetic susceptibility and P-wave velocity in core samples from the Taiwan  
665 Chelungpu-Fault Drilling Project (TCDP). *Journal of Structural Geology* 30(8): 948-962.
- 666 Mattei, M., F. Speranza, A. Argentieri, F. Rossetti, L. Sagnotti and R. Funicello, 1999.  
667 Extensional tectonics in the Amantea basin (Calabria, Italy): a comparison between structural  
668 and magnetic anisotropy data. *Tectonophysics* 307(1): 33-49.
- 669 Mattei, M., Sagnotti, L., Faccenna, C., Funicello, R., 1997. Magnetic fabric of weakly  
670 deformed clay-rich sediments in the Italian peninsula: Relationship with compressional and  
671 extensional tectonics. *Tectonophysics* 271, 107-122.
- 672 Matray, J. M., S. Savoye and J. Cabrera, 2007. Desaturation and structure relationships around  
673 drifts excavated in the well-compacted Tournemire's argillite (Aveyron, France). *Engineering*  
674 *Geology* 90(1): 1-16.
- 675 Mennessier, G., and P. Collomb, 1983, Carte géologique de la France 1/50000—Millau  
676 Larzac Ouest-Roquefort, Bur. Rech. Géol. et Minières, Orléans, France.

- 677 Moore D.M., Reynolds R.C., 1989. X-ray diffraction and the identification and analysis of  
678 clay minerals. Oxford University Press, - New York.
- 679 Muxworthy, A.R., Williams, W., 2009. Critical superparamagnetic/single-domain grain sizes  
680 in interacting magnetite particles: implications for magnetosome crystals. *Journal of The*  
681 *Royal Society Interface* 6, 1207-1212.
- 682 Özdemir, Ö., Dunlop, D.J., Moskowitz, B.M., 2002. Changes in remanence, coercivity and  
683 domain state at low temperature in magnetite. *Earth and Planetary Science Letters* 194, 343-  
684 358.
- 685 Parés, J. M., 2004. How deformed are weakly deformed mudrocks? Insights from magnetic  
686 anisotropy. Geological Society, London, Special Publications 238(1): 191-203.
- 687 Parés, J.M., 2015. Sixty Years of Anisotropy of Magnetic Susceptibility in deformed  
688 sedimentary rocks. *Frontiers in Earth Science* 3.
- 689 Parés, J.M., van der Pluijm, B.A., Dinarès-Turell, J., 1999. Evolution of magnetic fabrics  
690 during incipient deformation of mudrocks (Pyrenees, northern Spain). *Tectonophysics* 307, 1-  
691 14.
- 692 Parés, J. M., N. J. C. Hassold, D. K. Rea and B. A. van der Pluijm, 2007. Paleocurrent  
693 directions from paleomagnetic reorientation of magnetic fabrics in deep-sea sediments at the  
694 Antarctic Peninsula Pacific margin (ODP Sites 1095, 1101). *Marine Geology* 242(4): 261-  
695 269.
- 696 Peyaud, J.-B., Pagel, M., Cabrera, J., Pitsch, H., 2006. Mineralogical, chemical and isotopic  
697 perturbations induced in shale by fluid circulation in a fault at the Tournemire experimental  
698 site (Aveyron, France). *Journal of Geochemical Exploration* 90, 9-23.
- 699 Rahe, B., D. A. Ferrill and A. P. Morris, 1998. Physical analog modeling of pull-apart basin  
700 evolution. *Tectonophysics* 285(1): 21-40.
- 701 Rochette, P., Fillion, G., Dekkers, M.J., 2011. The Low-Temperature Magnetic Transition of  
702 Monoclinic Pyrrhotite. *The IRM Quarterly* 21.
- 703 Rochette, P., Fillion, G., Mattei, J.L., Dekkers, M.J., 1990. Magnetic transition at 30-34 K in  
704 pyrrhotite-insigh into a widespread occurrence of this mineral in rocks. *Earth and Planetary*  
705 *Science Letters* 98, 319-328.
- 706 Rossetti, F., Aldega, L., Tecce, F., Balsamo, F., Billi, A., Brilli, M., 2011. Fluid flow within  
707 the damage zone of the Boccheggiano extensional fault (Larderello–Travale geothermal field,  
708 central Italy): Structures, alteration and implications for hydrothermal mineralization in  
709 extensional settings. *Geological Magazine* 148, 558-579.
- 710 Savoye, S., Michelot, J.L., Altinier, M.V., Lemius, S., 2008. Origin of pore-water isotopic  
711 anomalies near fractures in the tournemire shales. *Physics and Chemistry of the Earth, Parts*  
712 *A/B/C* 33, Supplement 1, S87-S94.

- 713 Sellin, P. and O. X. Leupin, 2013. The use of clay as an engineered barrier in radioactive-  
714 waste management – a review. *Clays and Clay Minerals* 61(6): 477-498.
- 715 Singsoupho, S., T. Bhongsuwan and S.-Å. Elming, 2015. Palaeocurrent direction estimated in  
716 Mesozoic redbeds of the Khorat Plateau, Lao PDR, Indochina Block using anisotropy of  
717 magnetic susceptibility. *Journal of Asian Earth Sciences* 106: 1-18.
- 718 Smirnov, A., 2009. Grain size dependence of low-temperature remanent magnetization in  
719 natural and synthetic magnetite: Experimental study. *Earth, Planets and Space* 61, 119-124.
- 720 Verwey, E. J. W. (1939). "Electronic Conduction of Magnetite (Fe<sub>3</sub>O<sub>4</sub>) and its Transition  
721 Point at Low Temperatures." *Nature* 144: 327.

Figure (with caption below and on the same page)

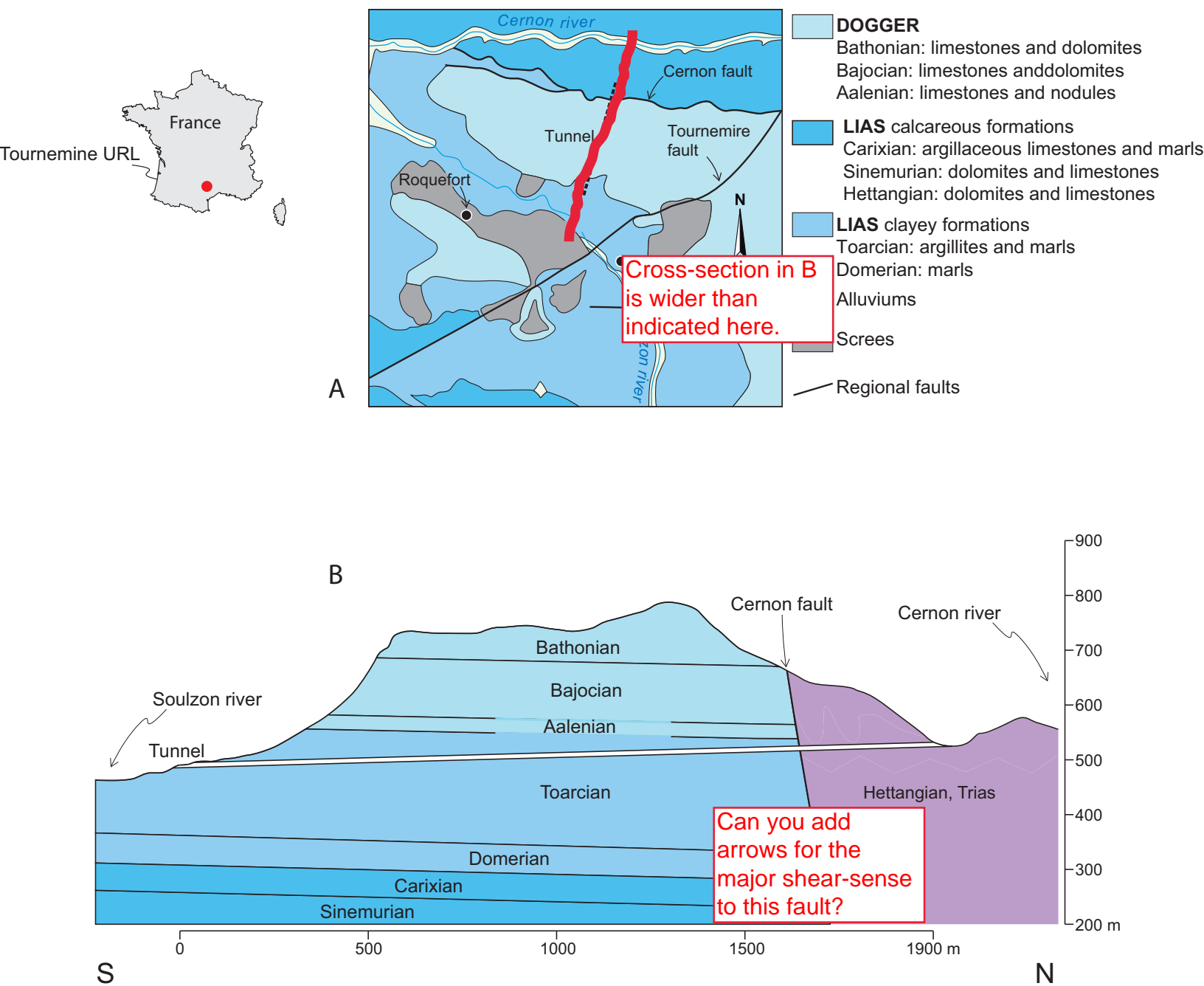


Figure 1: (A) Location of the Tournemire site: simplified geological map after Mennessier and Collomb (1983). (B) Geological cross-section of the Tournemire experimental station (Cabrera, 2002).



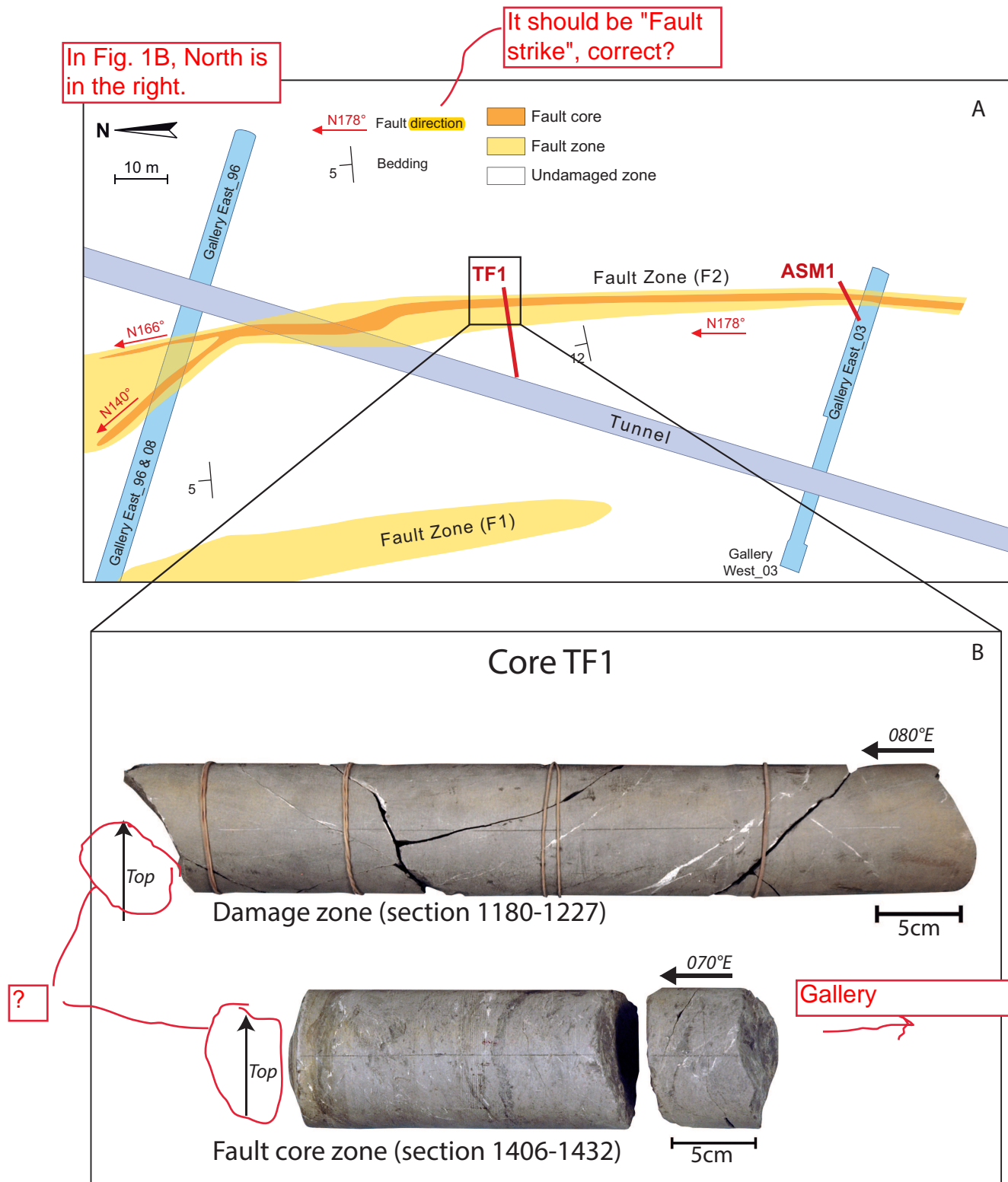


Figure 2: (A) Simplified map of the Tournemire Underground Research Laboratory and cores TF1 and ASM1 location (Dick et al. 2016). (B) Picture of sections 1180-1227 (damage zone) and 1406-1432 (fault core) from TF1.

Figure (with caption below and on the same page)

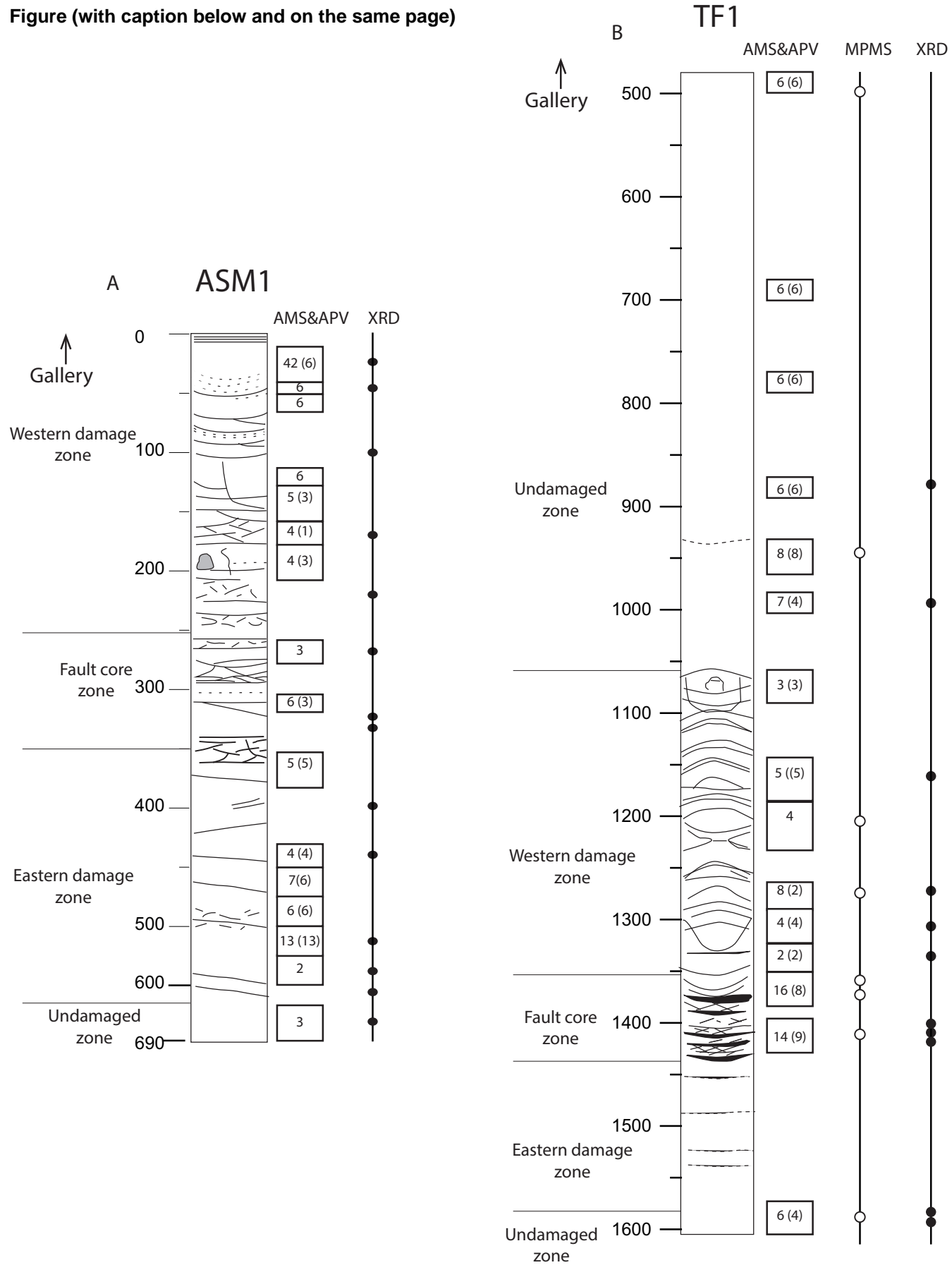


Figure 3: Logs of ASM1 (A) (société Martinez and Pierre Dick, personal communication) and TF1 (B) (Cofor - GeoSonic France for the IRSN) made during the drilling process. The spatial distribution of the undamaged, damage and fault core zones was determined on observation criteria during the core logging. The number cubes for ASM and (APV) are indicated. The black and white circles correspond respectively to the near shear points in where the powder samples were collected for the XRD and low-T SIRM measurements.

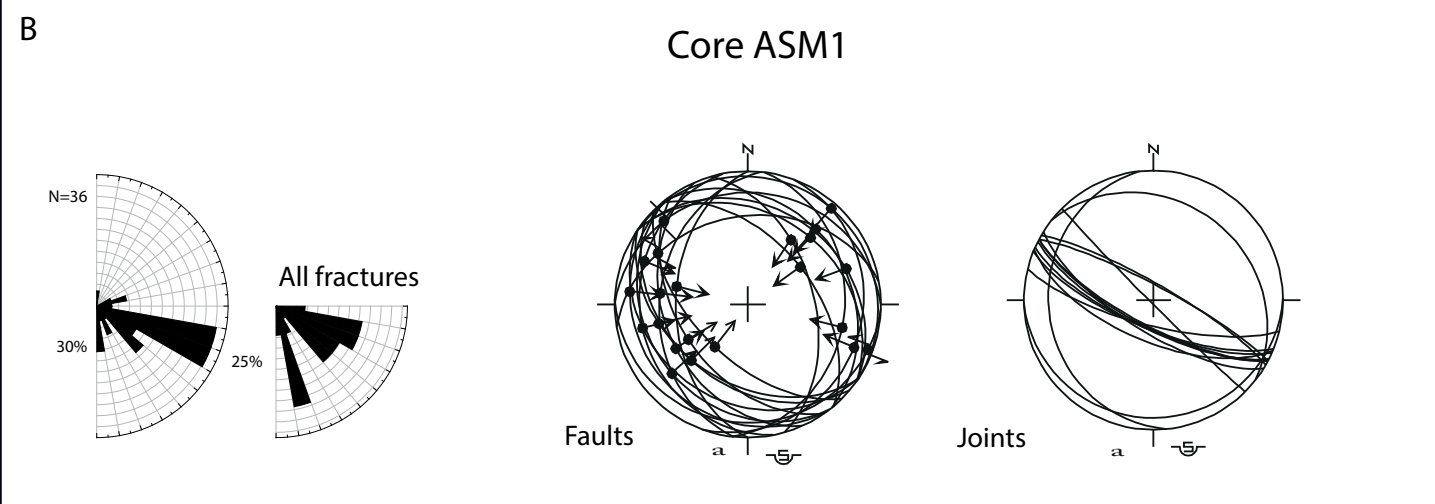
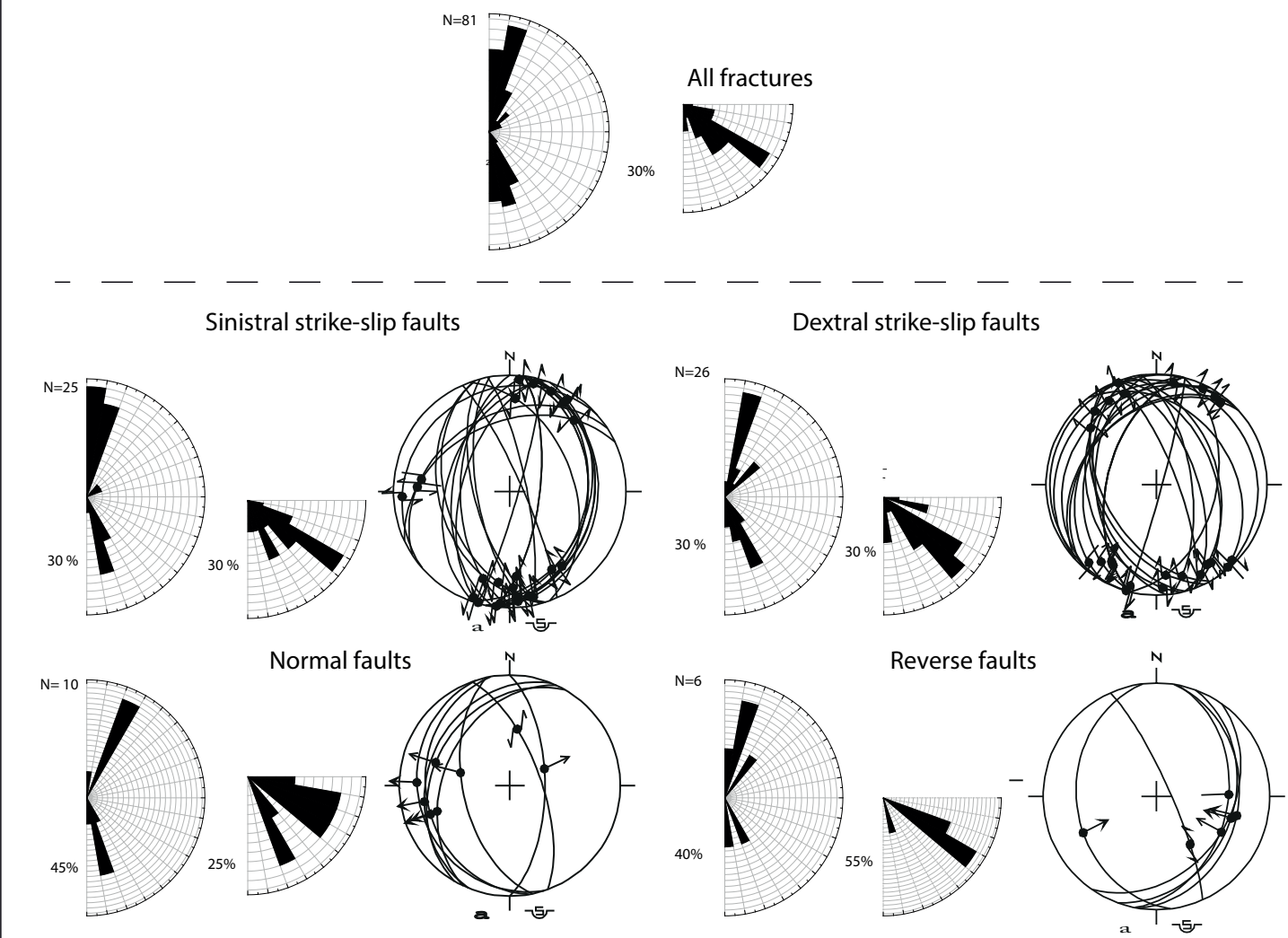


Figure 4: Stereographic projection (lower hemisphere, equal-area projection) showing the orientation and striae of the fault planes measured in TF1 and ASM1 cores. (A) Rose diagrams of the fault strike and fault dip for all the fractures in core TF1. Rose diagrams and paleo-stress orientation determined by slickensides analyses for: Sinistral strike-slip faults, dextral strike-slip faults, normal faults and reversal faults. (B) Rose diagrams of the fault strike and fault dip in core ASM1. Paleo-stress orientation determined by slickensides analyses for faults and joints. Lines: fault planes. Slickenside lineations in dots with double arrows for strike-slip motion and with outward-directed or inward-directed single arrow for normal or reverse motion. The fault surfaces measured in F2 fault zone show a main N-S trend, but various orientation and sense of the slip vector. See in text for further explanation.

Figure (with caption below and on the same page)

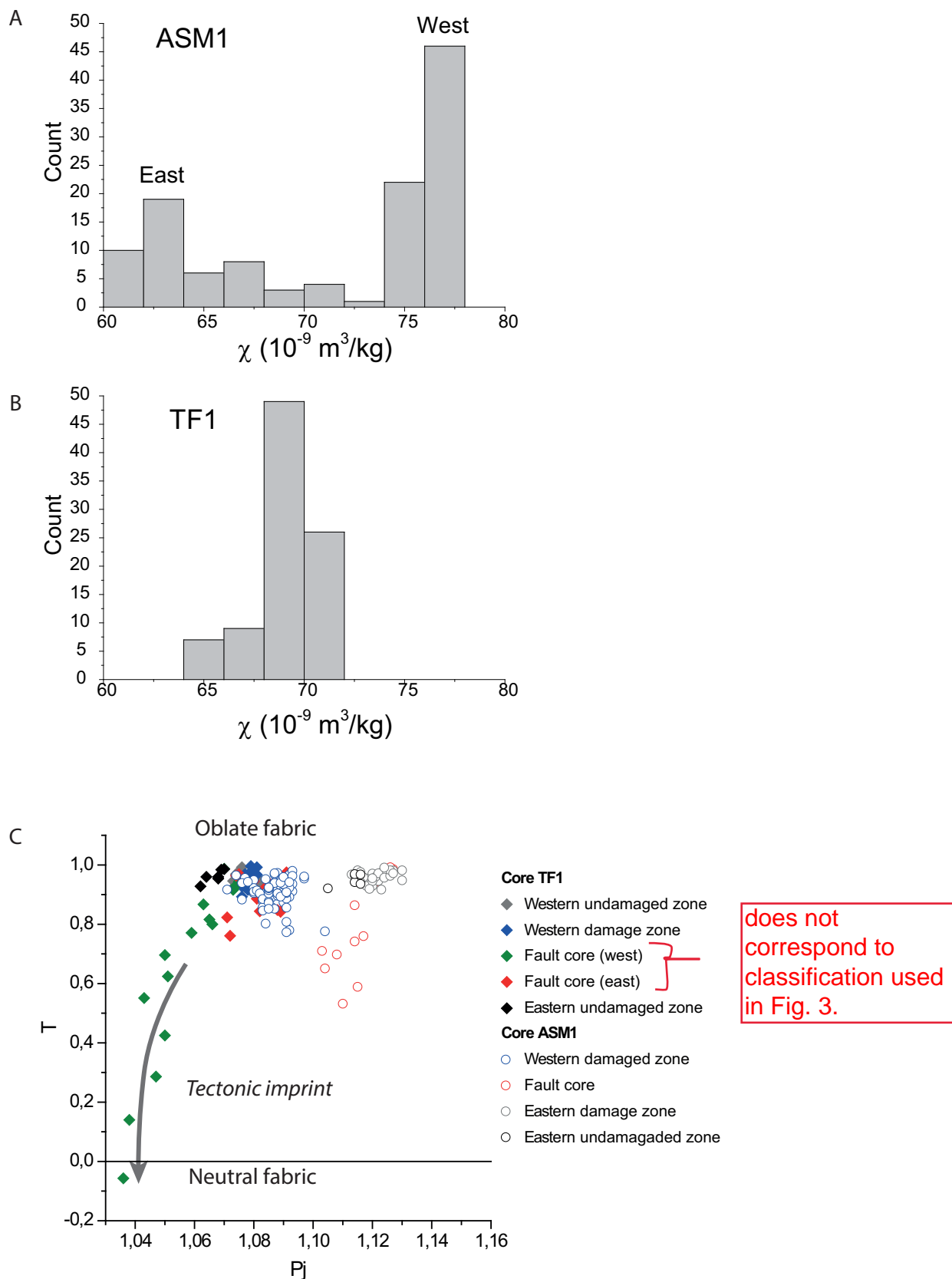


Figure 5: Histogram of density normalised magnetic susceptibility for cores ASM1 (A) and TF1 (B). Jelinek diagram for cores TF1 and ASM1 showing the evolution of the ASM shape parameter (T) versus the degree of anisotropy (Pj) (C).

Figure (with caption below and on the same page)

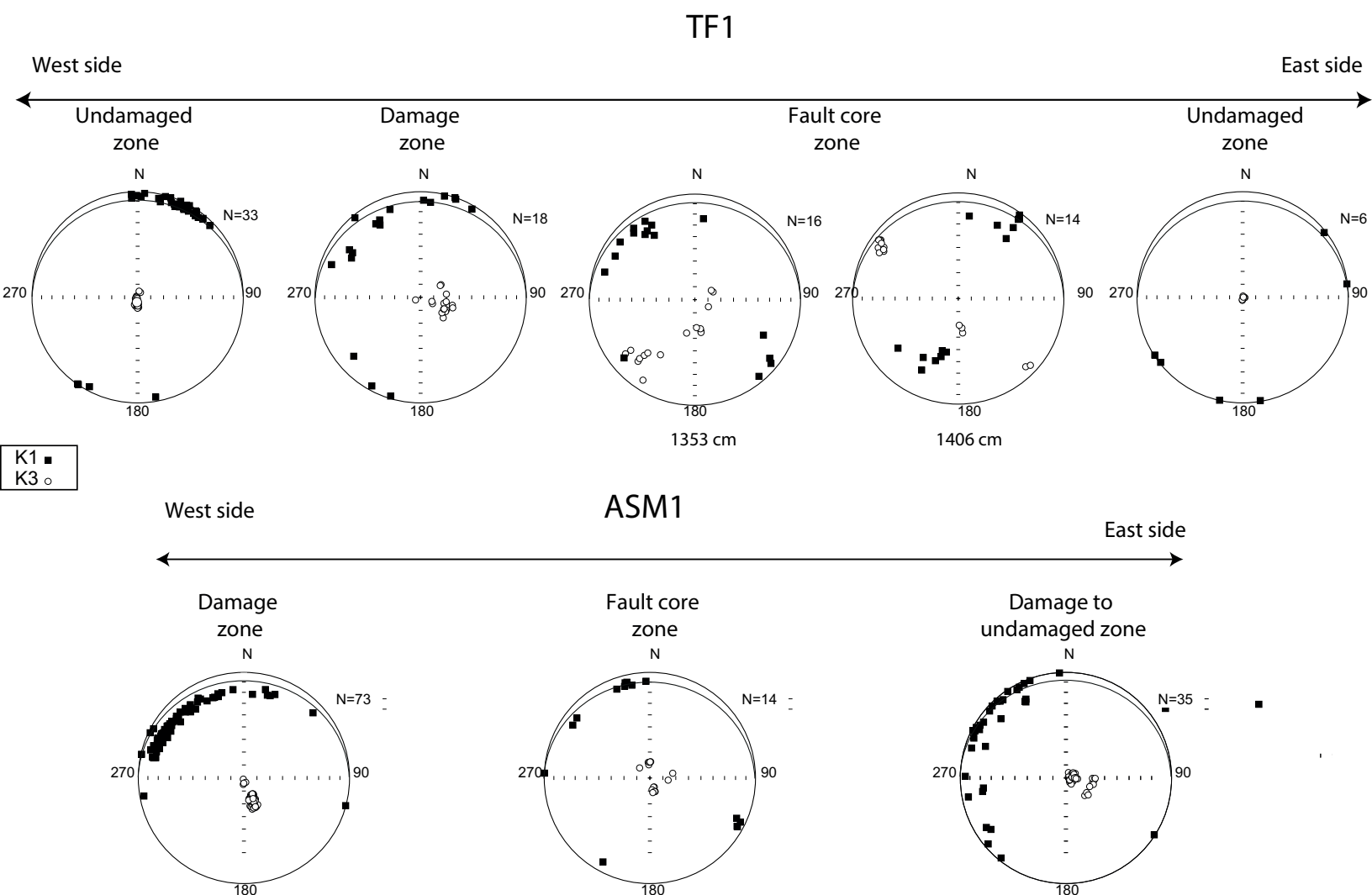


Figure 6: Equal-area lower-hemisphere stereograms in geographical coordinate system of the principal AMS axes for the undamaged zone, damage zone and fault core zone of cores TF1 and ASM1. White circles represent K3 axes, triangles and black squares represent K1 axes. The black line represents a bedding plane oriented to the north with a  $10^\circ$  dip which corresponding to the values measured in the undamaged zone.

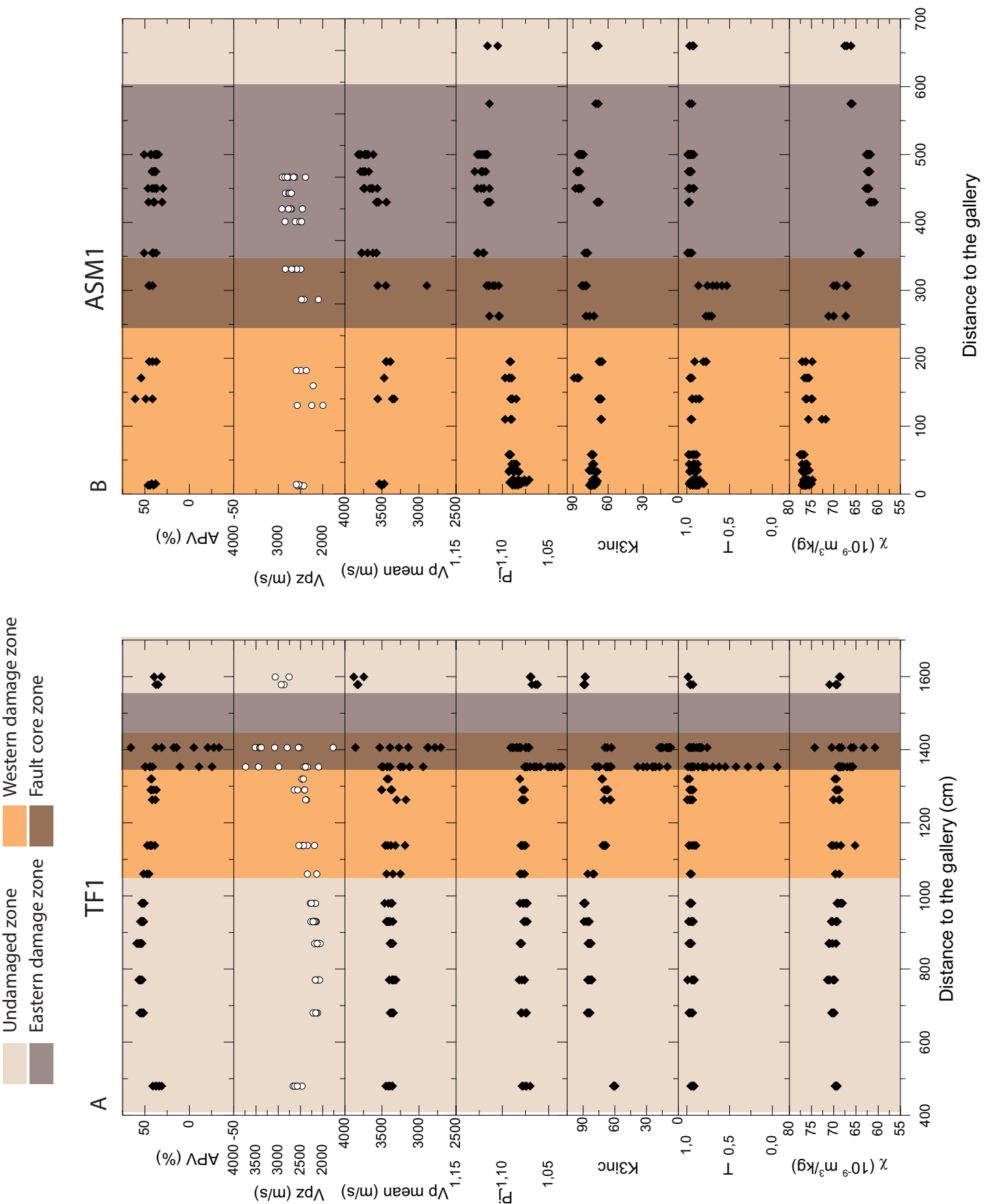


Figure 7: Evolution of magnetic susceptibility normalized by the density ( $\text{m}^3/\text{kg}$ ), shape parameter T, degree of anisotropy  $P_j$ ; K3 inclination, mean  $P_p$  ( $V_{pm}=(V_{px}+V_{py})/2$ );  $V_{pz}$  (m/s) and % APV for core TF1 (A) and ASM1 (B) across the undamaged, damage and the fault core zones.

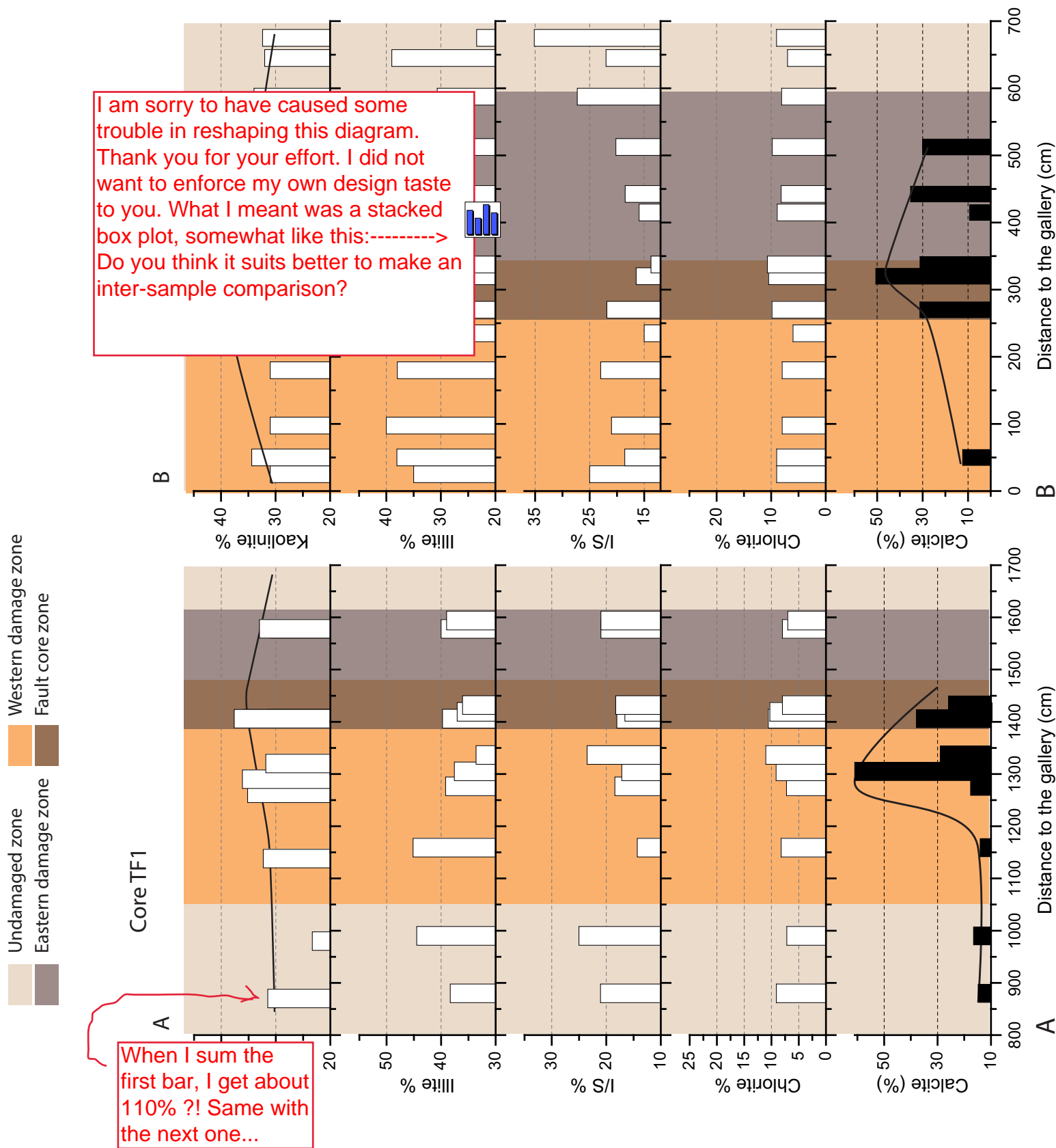
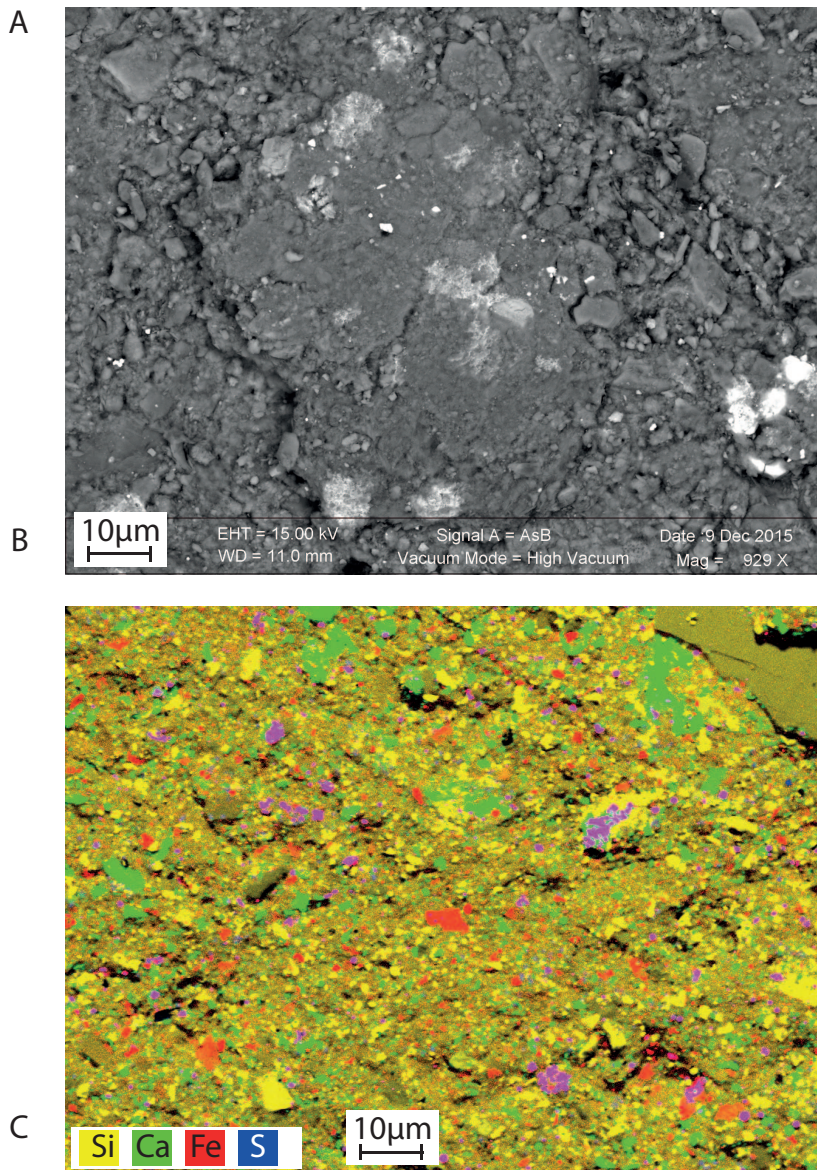


Figure 8: Stacked box plot indicating the relative proportions of calcite and of the various clay minerals in cores TF1 and ASM1 across the undamaged, damage and the fault core zones. The main trend observed in calcite and kaolinite measurements is indicated by a black line.



I do not think that this figure is necessary. It would be nice if there were a comparison between samples, e.g. from the damaged zone or the fault core.

Figure 9: (A) SEM image of a broken surface in core TF1, section 980-1000 (undamaged zone). (B) Si, S, Fe, Ca elements mapping of the same sample. Silicates, calcites, pyrites and small quantities of iron carbonates were observed. (C) EDS spectrum of iron rich carbonate observed in SEM image.



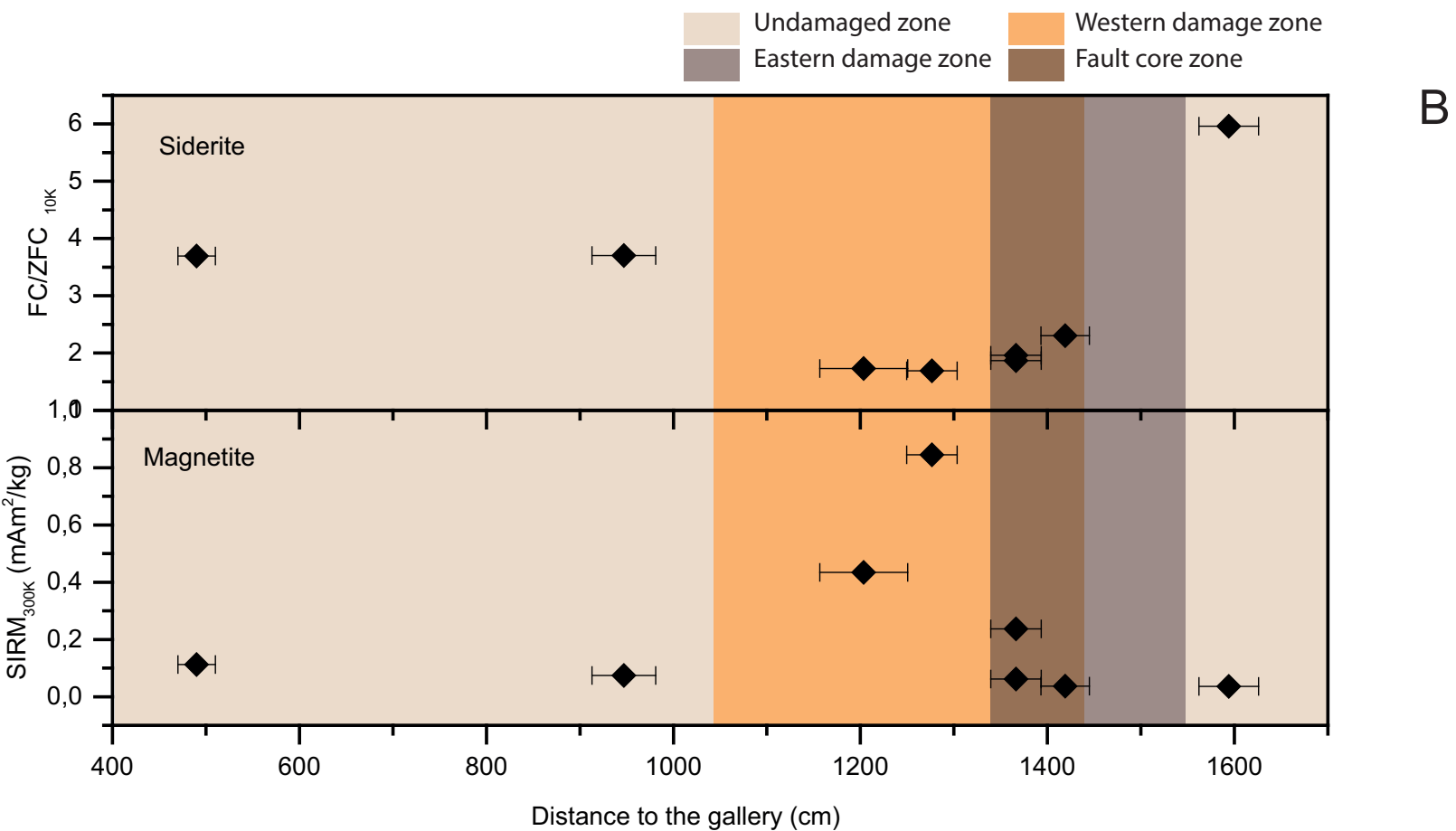
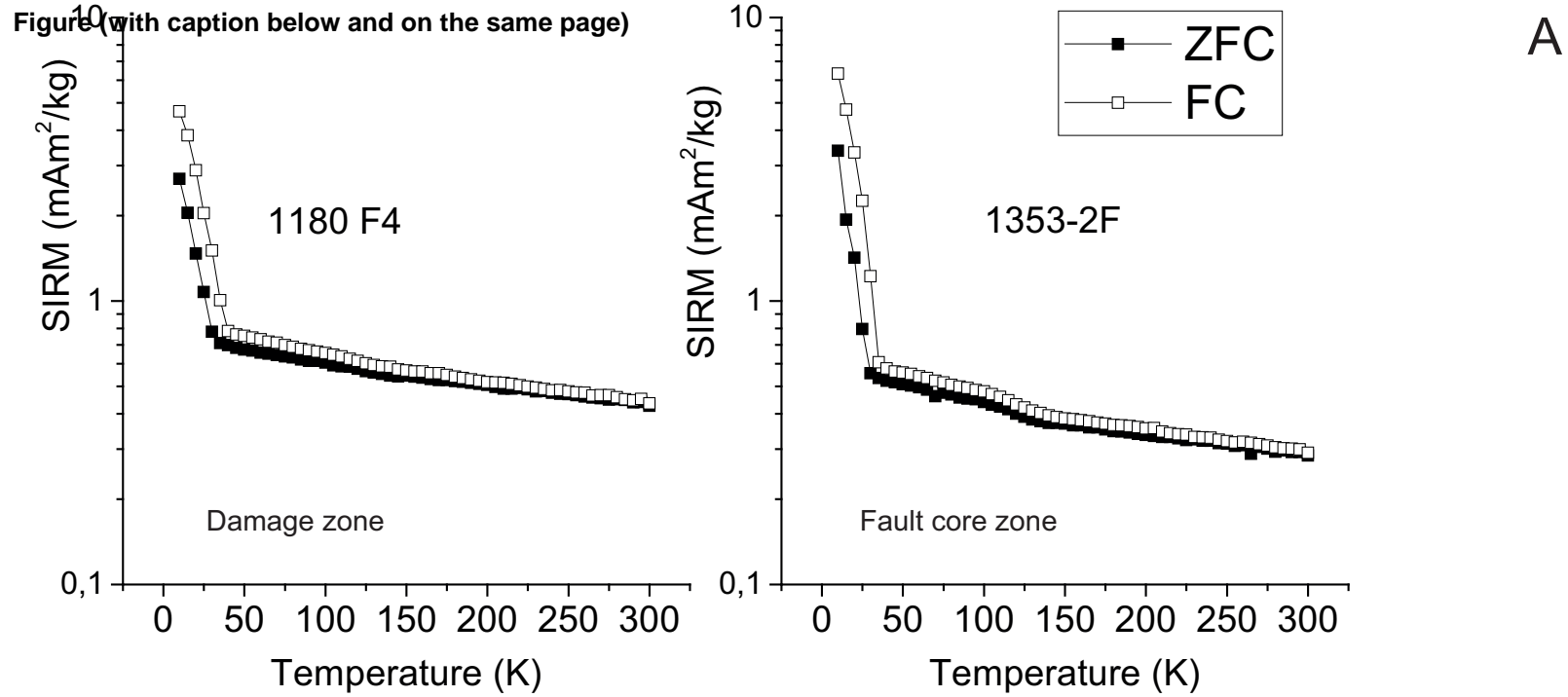


Figure 10: LT-SIRM warming curves measured in powders from the fracture planes in the damage zone (sample 1180) and fault core zone (sample 1353) in core TF1. FC (Field cool) and ZFC (Zero field curve) correspond respectively to samples cooled at zero field and a field of 2.5T. (B) Evolution of the SIRM at room temperature (SIRM<sub>300K</sub>) and FC/ZFC ratio at 10K across the undamaged, damage and the fault core zones.

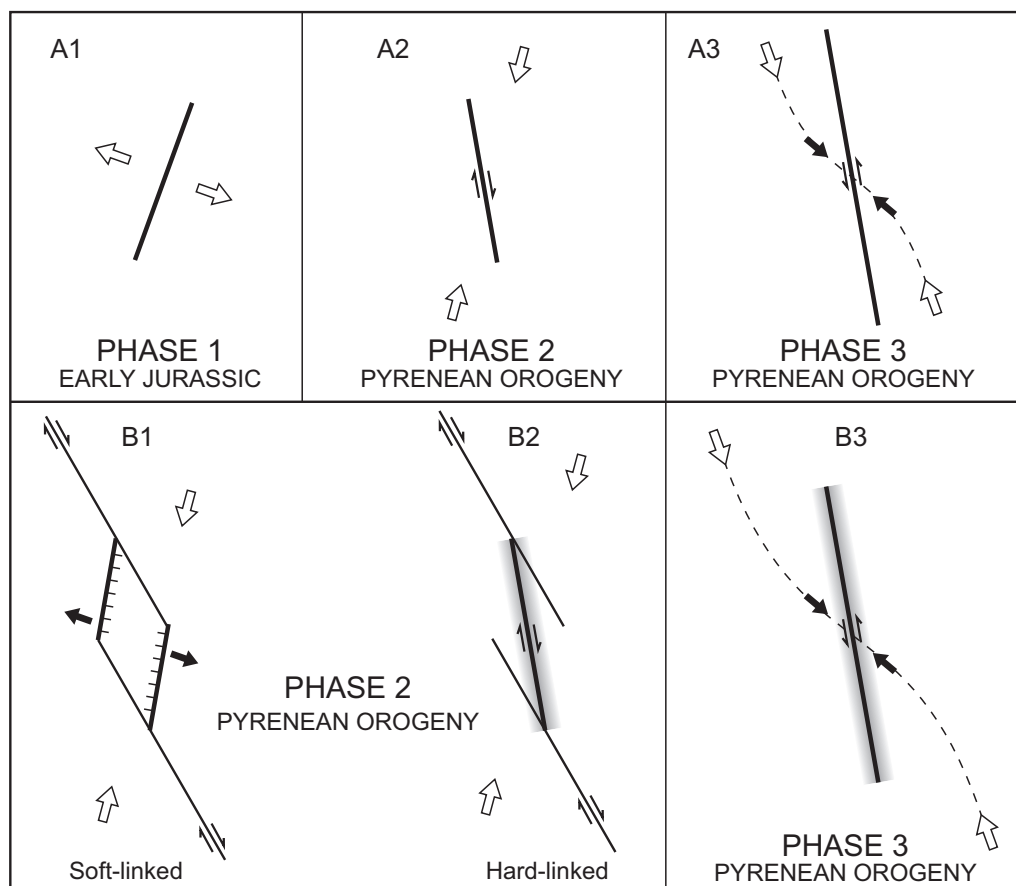


Figure 11: Alternative scenario for the time evolution of F2 fault zone in the Tournemire Gallery. In A, F2 fault first formed as a normal fault during the Early Jurassic extensional tectonics (A1) and was later reactivated during the Pyrenean orogeny. Due to the counterclockwise rotation of the Pyrenean compression through time, F2 first slipped as a dextral fault (A2) and then as a sinistral fault (A3). In B, all fractures found in F2 zone resulted from its strike-slip movement during the Pyrenean orogeny. B1 and B2 represent the evolution of a relay between two NW-SE dextral fault segments. Normal faulting in this extensive relay was followed by branching of the two faults segments. Sinistral reactivation then occurred (B3) as the Pyrenean compression rotated counterclockwise as in A3.